

BOWIE-ALIGN: JWST reveals hints of planetesimal accretion and complex sulphur chemistry in the atmosphere of the misaligned hot Jupiter WASP-15b

James Kirk^{1,★}, Eva-Maria Ahrer², Alastair B. Claringbold^{3,4}, Maria Zamyatina⁵, Chloe Fisher⁶, Mason McCormack⁷, Vatsal Panwar^{3,4}, Diana Powell⁷, Jake Taylor⁶, Daniel P. Thorngren⁸, Duncan A. Christie², Emma Esparza-Borges^{9,10}, Shang-Min Tsai¹¹, Lili Alderson^{12,13}, Richard A. Booth¹⁴, Charlotte Fairman¹², Mercedes López-Morales¹⁵, N. J. Mayne⁵, Annabella Meech^{6,16}, Paul Mollière², James E. Owen¹, Anna B.T. Penzlin¹, Denis E. Sergeev⁵, Daniel Valentine¹², Hannah R. Wakeford¹², and Peter J. Wheatley^{3,4}

¹*Department of Physics, Imperial College London, Prince Consort Road, SW7 2AZ, London, UK*

²*Max-Planck-Institut für Astronomie, Königstuhl 17, 69117 Heidelberg, Germany*

³*Centre for Exoplanets and Habitability, University of Warwick, Gibbet Hill Road, Coventry CV4 7AL, UK*

⁴*Department of Physics, University of Warwick, Gibbet Hill Road, Coventry CV4 7AL, UK*

⁵*Department of Physics and Astronomy, Faculty of Environment, Science and Economy, University of Exeter, Exeter EX4 4QL, UK*

⁶*Department of Physics, University of Oxford, Denys Wilkinson Building, Keble Road, Oxford, OX1 3RH, United Kingdom*

⁷*Department of Astronomy & Astrophysics, University of Chicago, Chicago, IL 60637, USA*

⁸*Department of Physics and Astronomy, Johns Hopkins University, Baltimore, MD 21218, USA*

⁹*Instituto de Astrofísica de Canarias, E-38200 La Laguna, Tenerife, Spain*

¹⁰*Departamento de Astrofísica, Universidad de La Laguna, E-38206 La Laguna, Tenerife, Spain*

¹¹*Department of Earth and Planetary Sciences, University of California, Riverside, CA, USA*

¹²*University of Bristol, HH Wills Physics Laboratory, Tyndall Avenue, Bristol, UK*

¹³*Department of Astronomy, Cornell University, 122 Sciences Drive, Ithaca, NY 14853, USA*

¹⁴*School of Physics and Astronomy, University of Leeds, Leeds, LS2 9JT*

¹⁵*Space Telescope Science Institute, 3700 San Martin Drive, Baltimore, MD 21218, USA*

¹⁶*Center for Astrophysics | Harvard & Smithsonian, 60 Garden St, Cambridge, MA 02138, USA*

Accepted XXX. Received YYY; in original form ZZZ

ABSTRACT

We present a transmission spectrum of the misaligned hot Jupiter WASP-15b from 2.8–5.2 microns observed with JWST’s NIRSpec/G395H grating. Our high signal to noise data, which has negligible red noise, reveals significant absorption by H₂O (4.2 σ) and CO₂ (8.9 σ). From independent data reduction and atmospheric retrieval approaches, we infer that WASP-15b’s atmospheric metallicity is super-solar ($\gtrsim 15\times$ solar) and its C/O is consistent with solar, that together imply planetesimal accretion. Our GCM simulations for WASP-15b suggest that the C/O we measure at the limb is likely representative of the entire photosphere due to the mostly uniform spatial distribution of H₂O, CO₂ and CO. We additionally see evidence for absorption by SO₂ and absorption at 4.9 μ m, for which the current leading candidate is OCS, albeit with several caveats. If confirmed, this would be the first detection of OCS in an exoplanet atmosphere and point towards complex photochemistry of sulphur-bearing species in the upper atmosphere. These are the first observations from the BOWIE-ALIGN survey which is using JWST’s NIRSpec/G395H instrument to compare the atmospheric compositions of aligned/low-obliquity and misaligned/high-obliquity hot Jupiters around F stars above the Kraft break. The goal of our survey is to determine whether the atmospheric composition differs across two populations of planets that have likely undergone different migration histories (disc versus disc-free) as evidenced by their obliquities (aligned versus misaligned).

Key words: keyword1 – keyword2 – keyword3

1 INTRODUCTION

One of the main goals behind many exoplanet atmosphere observational programmes is to learn about exoplanet formation and evolu-

* E-mail: j.kirk22@imperial.ac.uk (JK)

tion. A primary focus of the field has been to use a planet’s carbon-to-oxygen ratio (C/O) to infer where a planet formed relative to ice lines in a protoplanetary disc, largely motivated by Öberg et al. (2011). However, there are many competing physical processes which make inferences from C/O challenging. These include the evolving ice lines within a disc (e.g. Morbidelli et al. 2016; Owen 2020), the drift of volatile-carrying solids in the disc (e.g., Booth et al. 2017; Schneider & Bitsch 2021), the relative importance of solid vs gaseous accretion in setting a planet’s atmospheric composition (e.g. Espinoza et al. 2017), and the diversity found from observations of protoplanetary discs (e.g., Law et al. 2021). Furthermore, it is likely that observations of exoplanetary atmospheres probe a limited range of atmospheric pressures (Dobbs-Dixon & Cowan 2017), which might not be representative of the bulk planet’s atmospheric composition due to processes such as local atmospheric mixing (e.g., Zamyatina et al. 2024), cloud formation (e.g., Helling et al. 2016), or a planet’s interior evolution (Müller & Helled 2024). Therefore, it remains to be observationally demonstrated that C/O, and atmospheric composition in general, are reliable tracers of planet formation.

As Penzlin & Booth et al. 2024 showed, the high dimensionality and unconstrained nature of key planet formation and disc parameters make it challenging to predict the atmospheric composition of an exoplanet from planet formation models. However, they demonstrated that comparing populations of planets with different migration histories could constrain planet formation models. Specifically, they showed that the C/O and metallicity of exoplanets that migrate through a disc should diverge from exoplanets that undergo disc-free migration, due to the fact that disc-migrated planets accrete inner disc material, a result that builds upon earlier work of Madhusudhan et al. (2014) and Booth et al. (2017). However, the amplitude and sign of this divergence is dependent on whether silicates from the inner disc release their oxygen into the planetary atmosphere upon accretion and the uncertain form of the dominant carbon carriers in discs.

These theoretical considerations motivate our observational survey which seeks to compare the compositions of four aligned/low-obliquity hot Jupiters that likely migrated through their protoplanetary discs versus four misaligned/high-obliquity hot Jupiters that likely underwent disc-free migration via high-eccentricity migration (e.g., Rasio & Ford 1996; Wu & Murray 2003; Ford & Rasio 2008; Muñoz et al. 2016). In our sample, we only include hot Jupiters orbiting F stars above the Kraft break (effective temperatures $\gtrsim 6100$ K) where tidal realignment is inefficient due to the stars’ radiative envelopes (e.g., Albrecht et al. 2012). This reduces the likelihood of our aligned sample being polluted with initially misaligned planets that have had their obliquities damped. Kirk et al. (2024a) gives more detail regarding our survey (‘BOWIE-ALIGN’, JWST program ID: GO 3838, PIs: Kirk & Ahler). By comparing aligned versus misaligned hot Jupiters, our goals are to constrain planet formation models (e.g., Penzlin & Booth et al. 2024) and to robustly test the reliability of C/O and metallicity as tracers of planet formation.

In this work, we present the first observations from our programme, those of the hot Jupiter WASP-15b. WASP-15b, discovered by West et al. (2009), has a mass of $0.542^{+0.054}_{-0.053} M_J$, a radius of $1.428 \pm 0.077 R_J$ (Bonomo et al. 2017), and an equilibrium temperature of 1676 ± 29 K (Southworth et al. 2013). Importantly for our programme, it has a precisely measured sky-projected obliquity ($\lambda = -139.6^{+4.3}_{-5.2}$, Triana et al. 2010) and orbits an F7 dwarf star above the Kraft break ($1.18 \pm 0.12 M_\odot$, $1.477 \pm 0.072 R_\odot$, Bonomo et al. 2017; $T_{\text{eff}} = 6372 \pm 13$ K, Gaia Collaboration et al. 2023). Our study is the first published transmission spectrum of WASP-15b.

We describe our observations in Section 2 and our data reduction in

Section 3 that results in the planet’s transmission spectrum (Section 3.3). In Section 4 we present constraints on the planet’s atmospheric metallicity derived from interior structure models. We interpret the transmission spectrum using 1D atmospheric models in Section 5, a 3D general circulation model in Section 6, and photochemical models in Section 7. We discuss our results in Section 8 and conclude in Section 9.

2 OBSERVATIONS

We observed one transit of WASP-15b on January 26, 2024 with the JWST/NIRSpec instrument (Jakobsen et al. 2022) in Bright Object Time Series mode. We used the G395H grating, the F290LP filter and the 2048 subarray. This setup covers opacity from H₂O, CO₂, CO and SO₂ (Alderson et al. 2023) between wavelengths of 2.8–5.2 μm at an average spectral resolution of $R = 2700$. We chose to use 44 groups per integration, which was informed by WASP-15’s K magnitude of 9.7, and we acquired 685 integrations over 7.72 hours, which included 2.26 hours pre- and 1.65 hours post-transit baseline. Due to the brightness of WASP-15, we used a nearby, fainter star for target acquisition (2MASS J13554509-3209041), observed with the SUB32 array and CLEAR filter.

3 DATA REDUCTION

We performed three independent reductions of the data, one using the Tiberius pipeline (Kirk et al. 2017, 2021) and the other two using the Eureka! pipeline (Bell et al. 2022). This approach was motivated by the work of the Early Release Science programme that demonstrated the benefits of independent data reductions (JWST Transiting Exoplanet Community Early Release Science Team et al. 2023; Alderson et al. 2023; Ahler et al. 2023; Feinstein et al. 2023; Rustamkulov et al. 2023). We give more information about our survey’s data analysis strategy in Kirk et al. (2024a). We describe the approaches taken by the independent reductions for this work in the following subsections.

3.1 Tiberius reduction

Tiberius (Kirk et al. 2017, 2021) is an open-source Python-based code that has been used in several studies of JWST data from multiple instruments (e.g., Rustamkulov et al. 2023; Alderson et al. 2023; Kirk et al. 2024b).

3.1.1 Light curve extraction

We began by processing the raw images (uncal . fits files) through the standard set of stage 1 steps¹ of the jwst pipeline (v1.8.2). However, we did not perform the jump step as it has been found to increase the noise in exoplanet transit light curves (e.g., Rustamkulov et al. 2023), and performed our own 1/f correction before the ramp_fit step. This involved subtracting the median value for each column on the detector after masking the 22 pixels centred on the stellar trace. The result of stage 1 was the production of gainscalestep . fits files with flux units of DN/s. We additionally performed the assign_wcs and extract_2d steps of the jwst pipeline to obtain the wavelength solution.

¹ https://jwst-pipeline.readthedocs.io/en/latest/jwst/pipeline/calwebb_detector1.html#calwebb-detector1

Next, we performed our own cosmic ray / bad pixel identification and removal. This was done by calculating the median value of every pixel in the time-series and replacing $> 5\sigma$ pixel outliers in the time-series with the median value for that pixel. We also generated our own bad pixel mask at this stage. To do this, we combined the pixels flagged during stage 1 as bad, saturated, dead or hot with pixels identified as 5σ outliers in a median-combined science integration from the first segment of data (260 integrations).

For each outlier-clipped integration, we then located the stellar trace by fitting a Gaussian to each row in the cross-dispersion direction, followed by a smoothing with a fourth order polynomial. We then performed standard aperture photometry with an aperture full width of 8 pixels, after subtracting the background flux which was calculated as the median of the 10 pixels after masking 22 pixels centred on the trace. We extracted the stellar flux between pixel rows 608 and 2044 (zero-indexed) for NRS1 and between rows 3 and 2043 for NRS2. With the stellar spectra in hand, we proceeded to create our light curves. For the white light curves, we integrated between wavelengths of 2.75 and 3.72 μm for the NRS1 detector and between 3.82 and 5.18 μm for the NRS2 detector. For our spectroscopic light curves, we adopted three different binning schemes: $R = 100$ (~ 61 pixels wide), $R = 400$ (~ 15 pixels wide) and 1 pixel resolution. Here we present results from the $R = 100$ and $R = 400$ analyses, with the high resolution (1-pixel) analysis presented in a follow-up study (Esparza-Borges et al., in prep.).

3.1.2 Light curve fitting

We fit the NRS1 and NRS2 white light curves independently to obtain our own set of system parameters, using a *batman* (Kreidberg 2015) analytic transit light curve model multiplied by a linear-in-time polynomial. The free parameters in our white light curve fits were: the time of mid-transit (T_0), the planet’s inclination (i), the planet’s semi-major axis relative to the stellar radius (a/R_*), the relative planet-to-star radii (R_p/R_*) and the two coefficients of the linear polynomial. We held the orbital period fixed to 3.7520998 days (Patel & Espinoza 2022) and the planet’s eccentricity to 0 (West et al. 2009). We used a quadratic limb darkening law and fixed the coefficients to the values computed by ExoTiC-LD (Grant & Wakeford 2024) using 3D stellar atmosphere models (Magic et al. 2015) and the stellar parameters from Bonomo et al. (2017) ($\log g = 4.17$ cgs, $[\text{Fe}/\text{H}] = -0.17$) and Gaia Collaboration et al. (2023) ($T_{\text{eff}} = 6372$ K).

We used a Levenberg-Marquadt algorithm, implemented through SciPy (Virtanen et al. 2020), to explore the parameter space and determine the best-fit parameters. For each light curve, we ran two sets of fits. The first fit allowed us to rescale the photometric uncertainties to give $\chi^2_{\nu} = 1$ for the best-fit model. The second fit was performed with the rescaled uncertainties. The results from this second fit were used in the rest of our analysis.

The results from our white light curve fits are shown in Figure 1 and Table 1. The system parameters from both detectors are consistent with one another and with values from TESS (Patel & Espinoza 2022). As shown by the Allan variance plots in Figure 2, the residuals from the white light curve fits show minimal red noise. This is likely due to a combination of the relatively high groups/integration of our observations (44), the choice to fill 80% of the full well and the relatively quiet nature of this F-type star. The Allan variance plots for the spectroscopic light curves are given in Appendix A and show that there is also minimal red noise in the spectroscopic light curves.

After the white light curve fits, we fit the spectroscopic light curves following the same procedure but with a/R_* , i and T_0 fixed to the

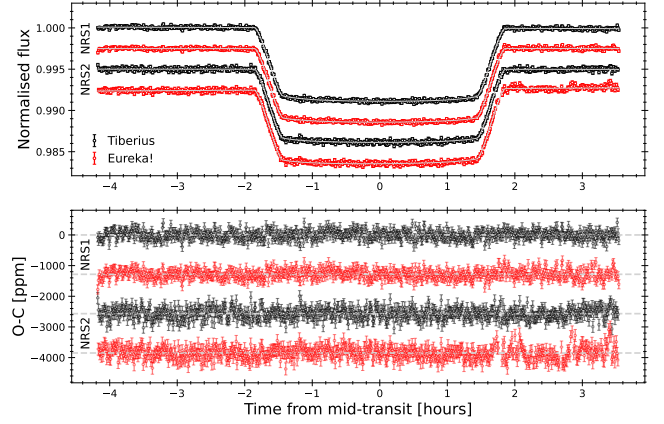


Figure 1. The white light curves and fits from two independent reductions. Top panel: the white light curves from Tiberius (black) and Eureka! (red). The thin grey lines indicate the best-fitting models. The light curves from NRS1 and NRS2 are offset from one another for visualisation. Bottom panel: the residuals from the fits in the top panel.

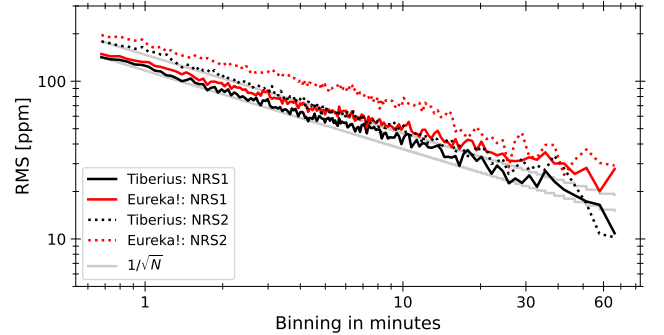


Figure 2. The Allan variance plot from the Tiberius (black) and Eureka! (red) white light curve fits. The results for NRS1 are shown by the solid lines and NRS2 by the dotted lines. These closely follow the expectations from pure white noise (grey lines) which indicates a lack of red noise in the residuals.

weighted mean values in Table 1. The spectroscopic light curves, models and residuals are shown in Figure 3.

3.2 Eureka! reduction

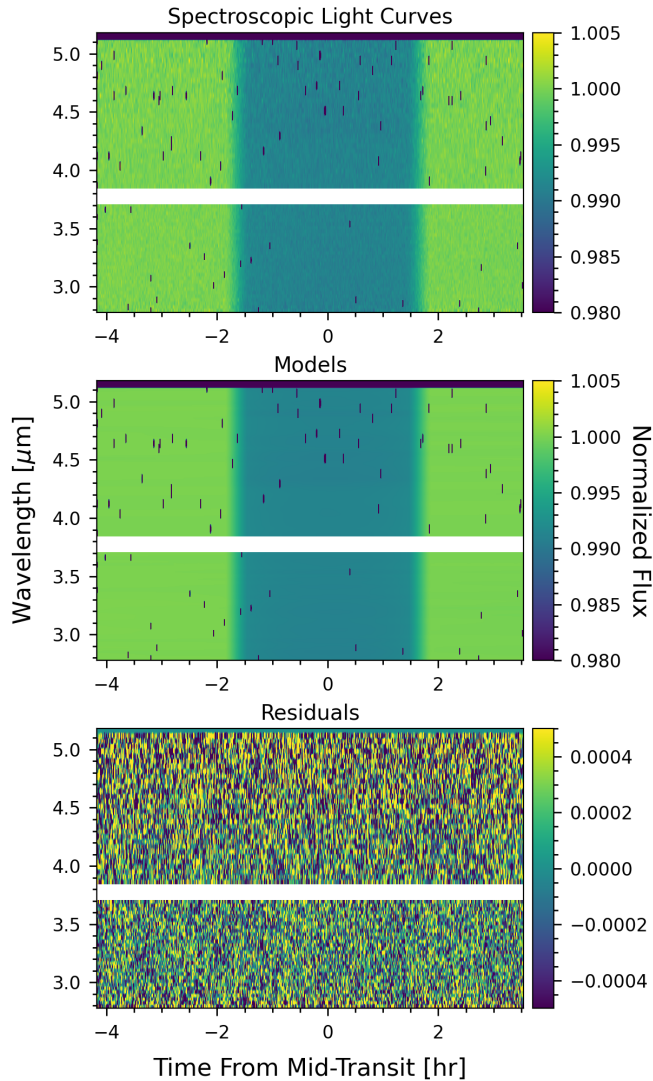
We utilised the open-source pipeline Eureka! (v0.11.dev245+ge8ea1d1c.d20240701; Bell et al. 2022) to reduce our data for two additional analyses. Eureka! has been successfully applied to JWST data sets and benchmarked against other pipelines (e.g., Ahrer et al. 2023; Moran et al. 2023). We describe the principal Eureka! reduction in the following section. The second Eureka! reduction was done independently with a different choice of reduction parameters and is presented in Appendix B.

3.2.1 Light curve extraction

We started our analysis with the raw images (uncl.fits files) and ran Stages 1 and 2 of Eureka!, which are wrapped around the default jwst pipeline (v1.12.2) steps. We followed the default steps similar

Table 1. The resulting system parameters from our fits to the JWST NIRSpec/G395H white light curves. We include the values from the TESS analysis of Patel & Espinoza (2022) for comparison.

Pipeline	Instrument	T_0 (BJD)	R_p/R_*	a/R_*	i ($^\circ$)
Tiberius	NRS1	$2460336.666378 \pm 0.000035$	0.092858 ± 0.000068	7.524 ± 0.033	86.160 ± 0.068
Tiberius	NRS2	$2460336.666412 \pm 0.000043$	0.092961 ± 0.000084	7.535 ± 0.042	86.184 ± 0.085
Tiberius	Weighted mean	$2460336.666392 \pm 0.000027$	0.092899 ± 0.000053	7.528 ± 0.026	86.167 ± 0.053
Eureka!	NRS1	$2460336.666404 \pm 0.000038$	0.093377 ± 0.000089	7.522 ± 0.064	86.130 ± 0.065
Eureka!	NRS2	$2460336.666484 \pm 0.000053$	0.093759 ± 0.000098	$7.545^{+0.035}_{-0.037}$	$86.217^{+0.070}_{-0.074}$
Eureka!	Weighted mean	$2460336.666441 \pm 0.000033$	0.093577 ± 0.000070	$7.536^{+0.023}_{-0.024}$	$86.177^{+0.047}_{-0.050}$
Patel & Espinoza (2022)	TESS	$2458610.70116 \pm 0.00026$	$0.0938^{+0.0009}_{-0.0012}$	$7.59^{+0.35}_{-0.28}$	$86.22^{+0.44}_{-0.63}$

**Figure 3.** The $R = 100$ spectroscopic light curves and fits from the Tiberius reduction. The horizontal white bars correspond to the wavelengths of the gap between the detectors. Top panel: the spectroscopic light curves for NRS1 and NRS2. Middle panel: the best-fitting light curve models. Bottom panel: the residuals from the light curve fits.

to the Tiberius but including the jump step with a threshold of 10σ which is larger than the *jwst* pipeline default value. We used the additional $1/f$ background subtraction at the group-level using the routine in *Eureka!* before the ramp fit and we opted to use a custom scale factor (using a smoothing filter calculated from the first group)

for the bias correction. We performed this step because it has been found to minimise transit depth offsets between the NRS1 and NRS2 detectors in other datasets (Moran et al. 2023).

Eureka!'s Stage 3 performs the spectral extraction of the data. First, we rejected outliers > 3 times the median absolute deviation in the spatial direction and performed double-iterative masking of $> 5\sigma$ outliers along the time axis. We also masked bad pixels flagged by the *jwst* pipeline's data quality (*dq_init*) step. This is followed by a correction for the curvature of the spectral trace and a median-subtraction of the background for each frame using the area > 8 pixels away from the central pixel of the spectral trace (i.e., masking the trace with a full width of 17 pixels). Then we used a full width of 9 pixels for the optimal spectral extraction.

The extracted spectra were generated and binned in Stage 4, where we clipped $> 5\sigma$ outliers from both NRS1 and NRS2 based on a rolling median of 5 pixels.

We followed the same binning schemes as in the Tiberius pipeline, i.e., we computed a broadband (white) light curve, as well as $R = 100$, $R = 400$ and pixel-level light curves. At this point we also generated limb-darkening coefficients using the same approach as in the Tiberius reduction.

3.2.2 Light curve fitting

In *Eureka!*'s Stage 5 we fit our extracted light curves using a *batman* transit light curve model (Kreidberg 2015) and a linear-in-time polynomial. We used the MCMC sampling algorithm *emcee* (Foreman-Mackey et al. 2013) where the starting parameter values were set to the results of an initial least-squares fit.

Similarly to the Tiberius reduction, we fit the NRS1 and NRS2 white light curves independently and retrieved the system parameters a/R_* , inclination and mid-transit time. Like Tiberius, we held the period fixed to 3.7520998 days (Patel & Espinoza 2022) and assumed a circular orbit. We used the quadratic limb-darkening law, where we fixed one parameter (*u1*) to the value obtained by the generated values by *ExoTiC-LD* and one (*u2*) was fitted in all light curve fits. The retrieved system parameters for NRS1 and NRS2 were fixed when fitting the spectroscopic light curves for the respective detectors. These system parameters are given in Table 1. The white light curves and best-fit models are shown in Figure 1. The Allan variance plots from the white light curve fits are shown in Figure 2 and the spectroscopic light curves in Figure A1.

3.3 The transmission spectrum of WASP-15b

Figure 4 shows WASP-15b's transmission spectrum at $R = 100$ and $R = 400$ from Tiberius and *Eureka!*. Other than a median transit depth difference of 38 ppm between the two pipelines' $R = 100$ spectra, there is excellent agreement between the spectra. After manually

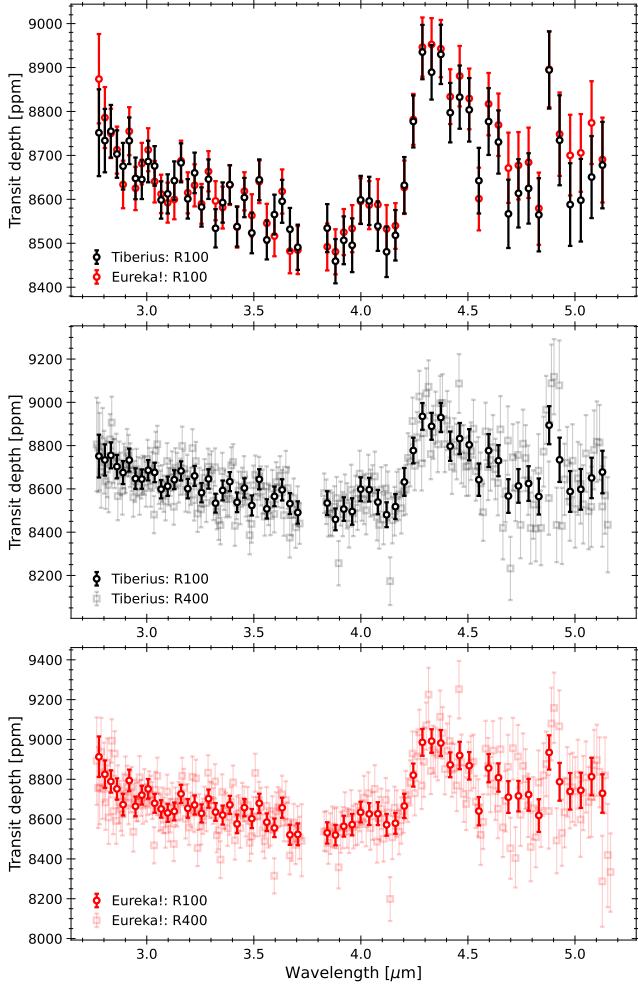


Figure 4. WASP-15b’s transmission spectrum. Top panel: the comparison between the spectra obtained with Tiberius (black) and Eureka! (red) at $R = 100$. The Eureka! spectrum has been offset by -38 ppm to match the median transit depth of Tiberius. Middle panel: The spectrum at $R = 100$ (black) and $R = 400$ (gray squares), both obtained with Tiberius. Bottom panel: The spectrum at $R = 100$ (red) and $R = 400$ (light red squares), both obtained with Eureka!.

correcting for the baseline transit depth offset, the residual median difference between the two pipelines’ spectra is 14 ppm which is $0.26\times$ the median 1σ transit depth uncertainty of 55 ppm. Looking beyond the agreement between the pipelines, the spectra reveal significant absorption features, which we explore in Sections 5 and 6.

4 CONSTRAINTS FROM INTERIOR STRUCTURE MODELS

Before we infer WASP-15b’s atmospheric metallicity from its transmission spectrum, we investigated plausible metallicities for this planet using the interior structure models of [Thorngren & Fortney \(2019\)](#). These models solve the 1D structure equations for giant planets, with the hot Jupiter heating power set according to [Thorngren & Fortney \(2018\)](#), and a metallicity prior set according to the mass-metallicity relation of [Thorngren et al. \(2016\)](#). In order to set an upper

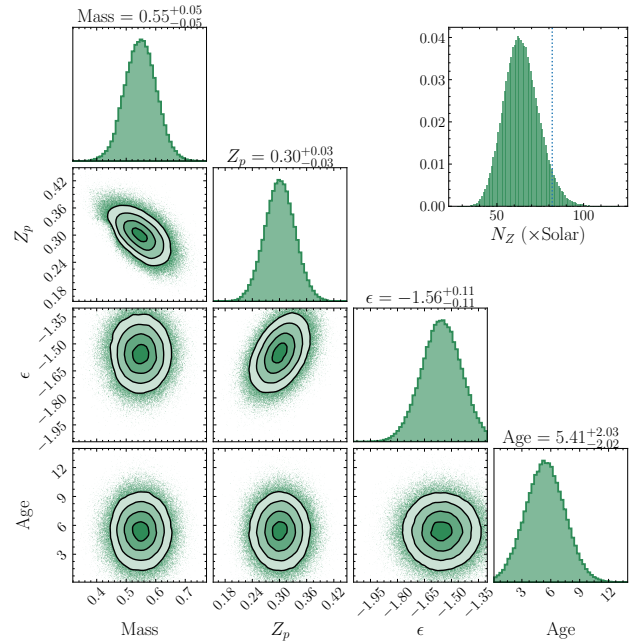


Figure 5. The posterior of the parameters of our interior structure model of WASP-15b: mass (M_J), Z_p (unitless mass ratio), ϵ (unitless heating power parameter), and the age (Gyr). The interior and statistical models used are identical to that of [Thorngren & Fortney \(2019\)](#). We find that the planet is moderately metal-rich with $Z_p = 0.30 \pm 0.03$, corresponding to a 95% upper limit on the atmospheric composition of $82\times$ solar.

limit on the potential atmospheric metallicity, these models assume a fully-mixed interior – no core to hide additional bulk metal.

Fitting the models to the observed mass, flux (irradiation), radius, and age, using the same Bayesian framework as [Thorngren & Fortney \(2019\)](#), we find that the bulk metallicity is $Z_p = 0.30 \pm 0.03$ in mass ratio (Figure 5). Note that this is the statistical uncertainty and does not account for theoretical uncertainties in e.g. the equations of state used. Still, it serves as a useful upper limit when converted from mass ratio to number ratio in \times solar units. Here we take the solar ratio of Z:H to be 0.00104, though note that other authors choose 0.00208 (solar composition gas under planetary conditions); it is important for consistency to be clear which definition is used. We find that the 95th percentile of the metallicity distribution is $82\times$ solar, corresponding to a mean molecular weight $\mu = 3.4$ amu, which we adopt as an upper limit on plausible atmospheric metallicities.

5 INTERPRETING THE SPECTRUM WITH 1D MODELS

In this section we describe the inferences we make from interpreting the spectrum with 1D atmospheric forward models and retrievals. We describe the results from three independent approaches in this Section and compare these in the Discussion (Section 8.1).

5.1 petitRADTRANS forward models

We implement a 1D forward model grid of synthetic transmission spectra using the `petitRADTRANS` package (v2.7.7, [Mollière et al. 2019](#); [Nasedkin et al. 2024](#)).

In both our forward models and retrievals with `petitRADTRANS` (Section 5.2), we use correlated- k radiative transfer with opacity

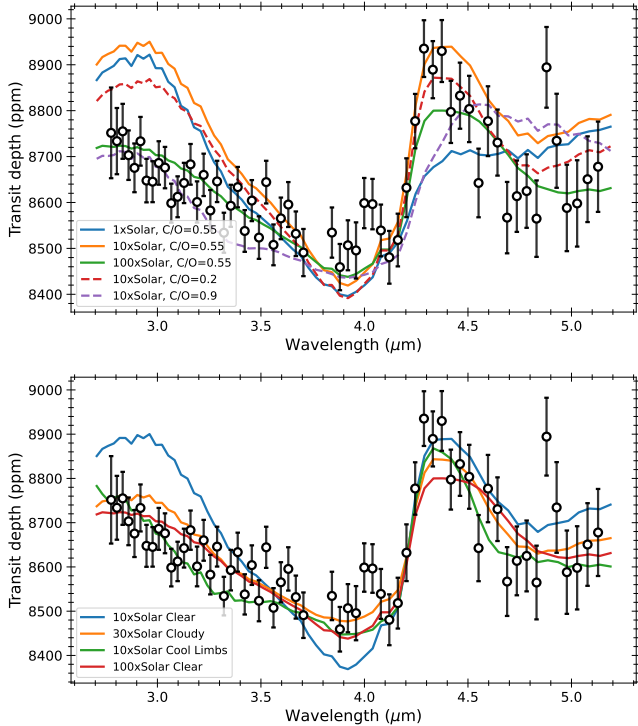


Figure 6. Top panel: Selected synthetic transmission spectra from our petitRADTRANS 1D equilibrium chemistry forward model grid, plotted against our Tiberius $R = 100$ spectrum of WASP-15b. The temperature profile is fixed to an isotherm at $T_{\text{eq}} = 1676$ K. We find that a \sim solar C/O ratio, and a metallicity $> 10\times$ solar is required to give the appropriate feature shapes, identifiable as H_2O and CO_2 , but we are not able to match the feature amplitudes with this simple model. Bottom panel: Selected synthetic transmission spectra from our expanded petitRADTRANS 1D equilibrium chemistry forward model grid. This demonstrates that the inclusion of higher altitude clouds at 0.1 mbar (the cloudy model, orange) or fixing the isothermal temperature to a cooler value of 1000 K (the cool limbs model, green), combined with a $10 - 50\times$ solar metallicity and $\text{C/O} = 0.55$ allows us to more successfully fit the feature amplitude compared to the original grid with no clouds and equilibrium temperature limbs (top panel).

tables at $R = 1000$ to calculate the transmission spectra. The opacity tables were pre-computed from spectral lines, using the following line-lists from HITEMP: H_2O and CO (Rothman et al. 2010b); and ExoMol: CO_2 (Yurchenko et al. 2020), SO_2 (Underwood et al. 2016), CH_4 (Yurchenko et al. 2017), H_2S (Azzam et al. 2016a), OCS (Owens et al. 2024), HCN (Barber et al. 2014), C_2H_2 (Chubb et al. 2021), SO (Brady et al. 2024), and NH_3 (Coles et al. 2019). We assume a H_2 - and He-dominated atmosphere and include opacity from H_2 - H_2 and H_2 -He collision-induced absorption as well as Rayleigh scattering from H_2 and He.

We use an initial grid of equilibrium chemistry simulations, with an isothermal temperature profile and the radius, mass, and equilibrium temperature of WASP-15b reported in Section 1, varying the C/O ratio from 0.1 – 1.0 and the metallicity from 0.1– $100\times$ solar. The equilibrium chemical composition is interpolated from a large grid pre-calculated using easyCHEM, as described in Mollière et al. (2017). We use the parametrization described in Mollière et al. (2015) using metallicity $[\text{Fe}/\text{H}]$ and C/O ratio. The abundance of all atoms, including the C/H ratio, is scaled by metallicity relative to solar (as

defined in Asplund et al. 2009), except the O/H ratio, which is further scaled by the C/O ratio relative to the C/H ratio.

Comparing this forward model grid by eye to both the Tiberius and Eureka! $R = 100$ spectra revealed that a super-solar metallicity of $10 - 100\times$ solar (Asplund et al. 2009), and a C/O ratio from 0.2 – 0.8 was required to give a similar spectrum, as seen in Figure 6 (top panel). Leaving out opacity from one molecule at a time from the model revealed H_2O and CO_2 as the primary opacity sources, with potential minor contributions from CO and H_2S . None of these clear atmosphere simulations were simultaneously able to predict the strength of the main H_2O and CO_2 features, with $< 80\times$ solar metallicity models over-predicting the strength of the H_2O feature, and $> 50\times$ solar metallicity models under-predicting the strength of the CO_2 feature. We therefore extended our grid with simulations with a grey cloud deck at 0.1 mbar, a grey cloud deck at 10 mbar, or a cooler 1000 K isothermal atmosphere. We found that 0.1 mbar clouds, a cooler terminator temperature, or some combination thereof create a good fit to both features, as portrayed in Figure 6 (bottom panel).

We were unable to generate satisfactory fits to the apparent features at $4.0\ \mu\text{m}$ and $4.9\ \mu\text{m}$ using equilibrium chemistry models. While the 0.1 mbar cloud models could effectively fit the $4.0\ \mu\text{m}$ feature in the Tiberius spectrum by increasing the continuum level to pass through the feature, the less cloudy models could not. Motivated by the detection of SO_2 at $4.0\ \mu\text{m}$ in the transmission of WASP-39b (Tsai et al. 2023), we tested this scenario for WASP-15b and found that the inclusion of a modest 2 ppm abundance of SO_2 can fit the feature, as described in Section 5.2. We tested a wide variety of molecules to explain the feature at $4.9\ \mu\text{m}$. We found that both OCS and O_3 had absorption centred at the right wavelengths but were generally broader than the feature width. We discuss the interpretation of this feature in more detail in Section 8.3. Using the TriArc package (Claringbold et al. 2023), we found that, given the equilibrium chemistry forward model and precision of the observation, the abundances of SO_2 and OCS would need to be ≥ 10 and 1 ppm to constitute 3σ detections.

5.2 petitRADTRANS retrievals

For a more detailed exploration of our transmission spectrum, we performed free chemistry and equilibrium chemistry retrievals on the $R = 100$ spectra from both Tiberius and Eureka!. petitRADTRANS uses Bayesian nested-sampling (Skilling 2004) implemented through MultiNest (Feroz & Hobson 2008) with PyMultiNest (Buchner et al. 2014). We used the same correlated- k opacities and isothermal temperature structure as the forward models of Section 5.1. We also included a grey cloud deck, with the cloud-top pressure as a free parameter, with a log uniform prior from $1\ \mu\text{bar}$ to 100 bar. We used a Gaussian prior for the planet’s gravity based on Bonomo et al. (2017), and wide, uniform priors for the planet’s radius ($0.8 - 1.8 R_J$) and limb temperature ($500 - 3000$ K). After experimenting with fitting the reference pressure at fixed planetary radius, we determined that a reference pressure of 1 mbar, at which the radius and gravity were defined, was most appropriate. The stellar radius was fixed to $1.477 R_\odot$.

For our free chemistry retrievals, we permitted the log volume mixing ratio to vary from -12 to -0.5 for each molecule. For our chemical equilibrium retrievals, the elemental ratios were parameterized by C/O ratio and metallicity, as previously described. We used a uniform prior of 0.1 to 1.5 for C/O, and a log uniform prior of -2 to 3 on metallicity. Given the strong impact of photochemistry on sulphur species, which is not accounted for by chemical equilibrium, we also ran a hybrid retrieval where the H_2O , CH_4 , CO , and

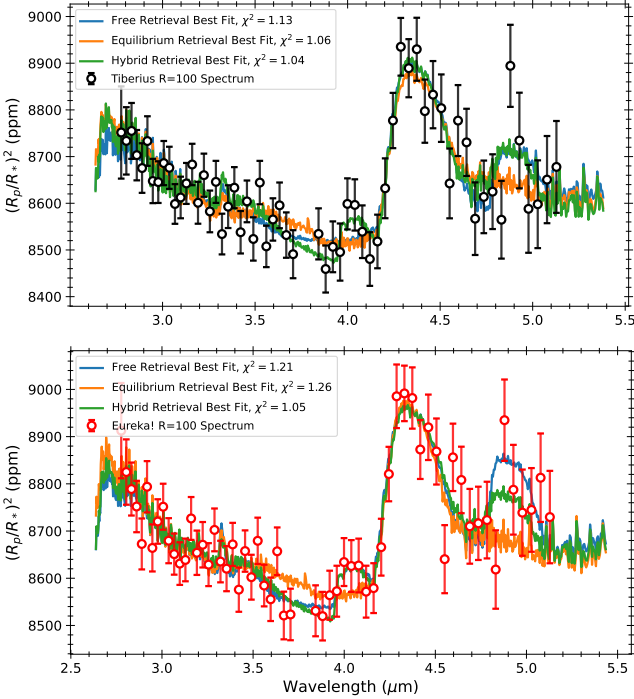


Figure 7. Best-fitting models from our *petitRADTRANS* free chemistry (blue), equilibrium chemistry (orange), and hybrid chemistry (equilibrium chemistry plus free S-bearing species, green) retrievals, fitted to the Tiberius $R = 100$ reduction (top panel) and Eureka! $R = 100$ reduction (bottom panel).

CO_2 abundances are determined by chemical equilibrium, while the photochemically-active sulphur species H_2S , SO_2 , and OCS abundances are free parameters.

For each pair of retrievals, we found complete consistency in the retrieved parameters between the Tiberius and Eureka! spectra. The complete retrieval results are summarised in Table E1. The best-fit models from each retrieval setup are shown in Figure 7.

Our equilibrium chemistry retrievals infer a C/O ratio of $0.48^{+0.11}_{-0.16}$ for the Tiberius spectrum and $0.53^{+0.09}_{-0.16}$ for the Eureka! spectrum, consistent with the solar value of 0.55 (using the solar metallicity of Asplund et al. 2009). The metallicity was determined to be super-solar, at 18^{+22}_{-8} solar and 22^{+27}_{-9} solar, respectively. We also retrieved a limb temperature of ~ 900 K, much colder than the equilibrium temperature, and minimal constraints on the cloud-top pressure, with a 3σ lower limit of 0.1 mbar.

Our free chemistry retrievals yielded similar results, ruling out H_2O and CO_2 abundances of less than 1 ppm. The log vertical mixing ratios were found to be $-2.83^{+0.59}_{-0.95}$ for H_2O and $-4.40^{+0.73}_{-1.02}$ for CO_2 in the Tiberius spectrum, with similar results for the Eureka! spectrum. There were no firm constraints for other species in the Tiberius spectrum, but the posterior corner plot from the Eureka! spectrum (see Figure E1) indicates that one of CO or OCS is likely present in the spectrum (the posteriors are inconsistent with neither being present to 3σ), but they cannot be distinguished. The upper limits of SO_2 and OCS are both above the respective 2 ppm and 0.2 ppm abundances that resulted in the best-fitting forward model in both retrievals. Our free chemistry retrievals favoured a cloudy atmosphere, placing a maximum cloud-top pressure of ~ 0.1 bar.

Our hybrid retrievals provided the best fit to the data, with reduced $\chi^2_V = 1.04$ for Tiberius and $\chi^2_V = 1.05$ for Eureka!, as depicted

Table 2. The Bayesian evidence ($\ln Z$) and degrees of freedom (DOF) from each of our *petitRADTRANS* retrievals, including equilibrium chemistry, free chemistry, and hybrid retrievals with equilibrium CH_4 , H_2O , CO , and CO_2 abundances, but the abundance of specified S-bearing species as free parameters. The evidence is very agnostic about the inclusion of various S-species in the Tiberius spectrum, but there is a moderate (2.6σ) preference for the hybrid chemistry model in the Eureka! spectrum, implying some combination of H_2S depletion, OCS enrichment, and the presence of SO_2 .

Retrieval	Tiberius $\ln Z$	Eureka! $\ln Z$	DOF
Equilibrium	-40.0	-47.5	6
Hybrid (H_2S only)	-39.9	-46.3	7
Hybrid ($\text{H}_2\text{S}+\text{SO}_2$)	-40.0	-46.0	8
Hybrid ($\text{H}_2\text{S}+\text{OCS}$)	-39.8	-45.7	8
Hybrid ($\text{H}_2\text{S}+\text{OCS}+\text{SO}_2$)	-40.3	-45.3	9
Free	-43.0	-48.2	11

in Figure 7. By treating the sulphur species as free parameters, we could fit the features at $4.0 \mu\text{m}$ and $4.9 \mu\text{m}$ with SO_2 and OCS , respectively, while also permitting H_2S to be depleted due to photochemical destruction or a low S/H ratio, impacting the spectrum either side of the detector gap. This approach resulted in more precise constraints on the C/O ratio, with a retrieved C/O ratio of $0.53^{+0.09}_{-0.15}$ for the Tiberius spectrum and $0.56^{+0.07}_{-0.13}$ for the Eureka! spectrum. The corner plot for the hybrid retrieval is shown in Figure 8.

We also ran additional retrievals for the purpose of model comparison. By running additional free chemistry retrievals omitting a single species on the Tiberius $R = 100$ spectrum and comparing the Bayesian evidence (Trotta 2008; Benneke & Seager 2013), we were able to place the detection significance of CO_2 at 8.9σ , and H_2O at 4.2σ . We also repeated the hybrid chemistry retrievals, omitting in turn SO_2 , OCS , and then both. We present a comparison of retrieval evidences in Table 2. In the Eureka! spectrum, $\Delta \ln Z = +2.2$ between the equilibrium and hybrid retrievals, equivalent to a 2.6σ preference. This is the result of small improvements of evidence, none of which are individually significant, from including each of H_2S , SO_2 , and OCS as free parameters. The Tiberius spectrum is agnostic between equilibrium and hybrid models, with a $\Delta \ln Z$ of only +0.5 between the best (hybrid with H_2S and OCS) and worst (hybrid with H_2S , SO_2 , and OCS) models.

5.3 BeAR retrieval

As a comparison, we also perform free-chemistry retrievals with the GPU-accelerated open-source Bern Atmospheric Retrieval code (BeAR²). This is an updated version of the retrieval code previously known as Helios-r2 (Kitzmann et al. 2020). BeAR uses the MultiNest library (Feroz & Hobson 2008) to perform the retrieval using Bayesian nested-sampling (Skilling 2004). It uses line-by-line opacity sampling, which we sampled at a resolution of 1.0 cm^{-1} in wavenumber (equivalent to $R \sim 2500$), and in this work we include the following molecules and their associated ExoMol line-lists: H_2O (Polyansky et al. 2018a), CH_4 (Yurchenko et al. 2013a), CO (Li et al. 2015a), CO_2 (Yurchenko et al. 2020), SO_2 (Underwood et al. 2016), H_2S (Azzam et al. 2016b), and OCS (Wilzewski et al. 2016). We also include opacity due to collision-induced absorption from $\text{H}_2\text{-H}_2$ (Abel et al. 2011) and $\text{H}_2\text{-He}$ (Abel et al. 2012), as well as Rayleigh scattering from H_2 (Vardya 1962). We assume free-chemistry, for which the molecular abundances are allowed to vary from volume mixing ratios of 10^{-12} to 1.0. The rest of the atmosphere is composed

² BeAR can be found at <https://github.com/newstrangeworlds/bear>

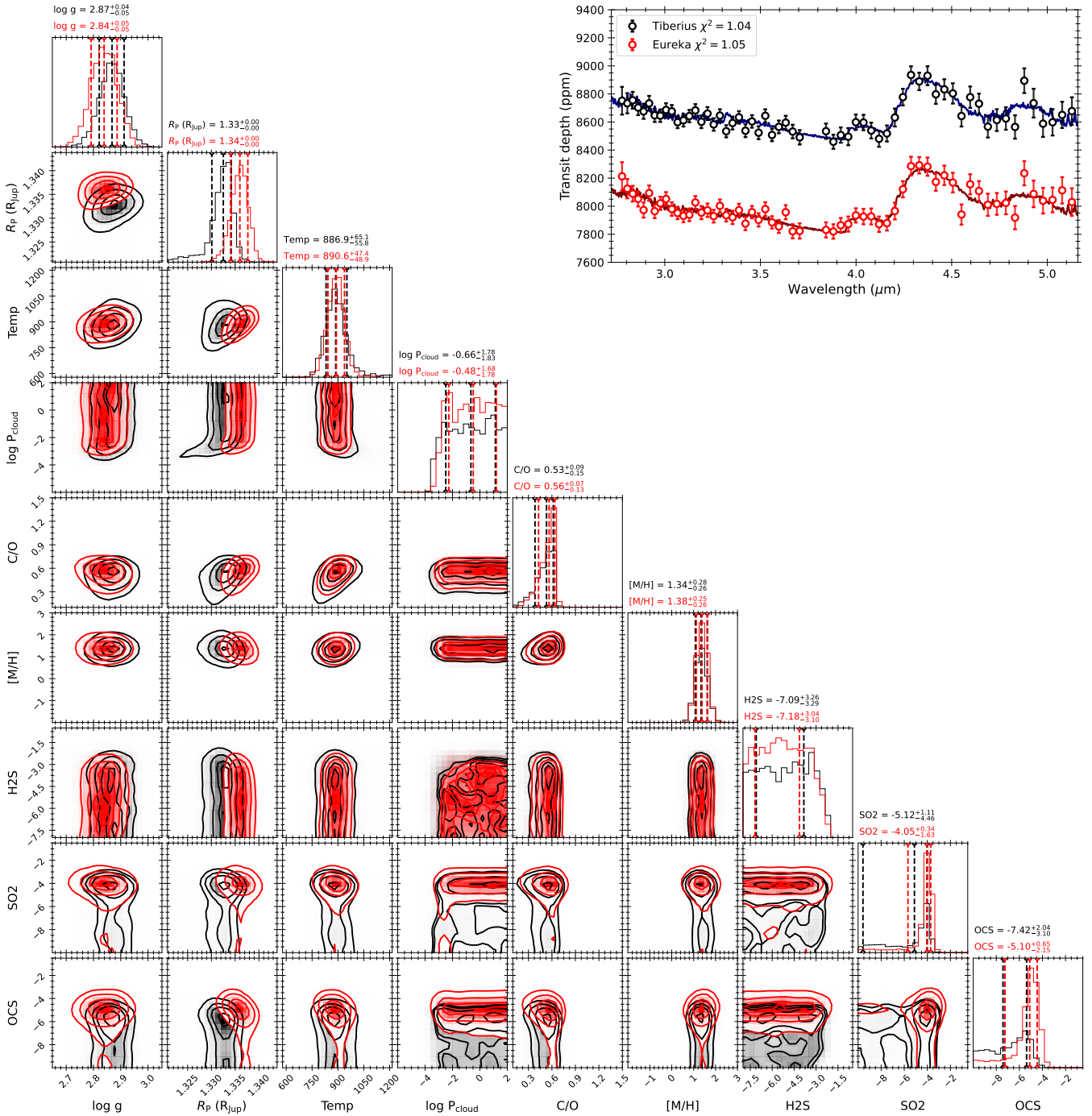


Figure 8. Corner plot showing the posterior PDFs from the hybrid petiRADTRANS retrieval performed on the Tiberius $R = 100$ spectrum (black) and Eureka! $R = 100$ spectrum (red). In the hybrid retrievals, the abundances of CH_4 , CO_2 , CO , and H_2O are fixed to their abundances at chemical equilibrium, while the abundances of S-bearing species H_2S , SO_2 , and OCS are free parameters. The best fitting model and residuals are displayed in the top right.

of H_2 and He, assuming a solar ratio of 0.17 (Asplund et al. 2009). The atmosphere is divided into 200 equal layers in log-pressure space, assuming a top pressure of 10^{-8} bar, and a bottom pressure of 10 bar. We assume an isothermal temperature, sampled between 500 and 2500 K, and include a grey cloud deck, for which we retrieve a cloud-top pressure sampled between 10^{-5} and 10 bar. The stellar radius is fixed to $1.477 R_\odot$, and the planet radius and gravity are free parameters. The planet radius uses a uniform prior of $1.27\text{--}1.40 R_J$,

and the gravity uses a Gaussian prior on $\log g$ with a mean of 2.828 and a standard deviation of 0.041, in cgs units. All BeAR retrievals in this work use 1000 live points.

We applied this retrieval code to both the Tiberius and Eureka! reductions at $R = 100$ and $R = 400$. For the $R = 100$ case (shown in Figure E2), we find a bimodal distribution for a number of parameters, representing two families of models. The first, favoured by the Eureka! data, is composed of H_2O , CO , and CO_2 , with a moderate

water volume mixing ratio of $\sim 10^{-5}$. The second, favoured by the Tiberius data, only shows evidence for H_2O and CO_2 , but now the water abundance is $\sim 15\%$. This corresponds to a very high-metallicity scenario, which is unphysical according to our interior structure model (see Section 4). For the $R = 400$ case, the retrieval favours the higher metallicity model in both reduction cases (not shown).

Motivated by the upper limits on WASP-15 b’s atmospheric metallicity and mean molecular weight derived from our interior structure model, we recomputed our BeAR posteriors after excluding the high metallicity modes from our posteriors. Specifically, we summed the mass mixing ratios of the molecules and limited the metal-mass ratio to 0.36 (equal to the 2σ upper limit on Z_p , Section 4). The resulting posteriors are shown in Figure 9. Now we see a good agreement between the Eureka! and Tiberius retrievals, with a water volume mixing ratio of $\sim 10^{-6}$. In agreement with `petitRADTRANS`, we retrieve limb temperatures of $\sim 900 - 1100$ K. The cloud-top pressure is unconstrained in both reduction cases. The upper-right insert of Figure 9 shows the best-fit spectra for each of the retrievals, as well as the reduced χ^2 values for these fits.

5.4 PLATON retrieval

We also used the open source PLATON package (Zhang et al. 2019, 2020) to interpret our transmission spectra. PLATON assumes equilibrium chemistry in 1D and an isothermal temperature-pressure profile. In its default configuration, which we used here, PLATON includes opacities from 34 chemical species with equilibrium abundances calculated using GGchem (Woitke et al. 2018) over a large grid of metallicities, C/O, temperatures, and pressures. The full list of species, along with line lists, is given in Zhang et al. (2020). The dominant species at the wavelengths and temperatures we are concerned with here are: H_2O (Polyansky et al. 2018a), CO_2 (Tashkun & Perevalov 2011) and CO (Faure et al. 2013; Gordon et al. 2017b). PLATON also includes SO_2 (Underwood et al. 2016) by default but not OCS which, as we discuss in Section 8.3, may be responsible for the feature at $4.9 \mu\text{m}$. For our analysis, we used the line lists generated at a spectral resolution of $R = 10000$ and the opacity sampling method of radiative transfer, rather than correlated- k .

In our PLATON retrievals we have five free parameters: the planet’s radius (R_p), the temperature of the isothermal atmosphere (T_{iso}), the atmospheric metallicity ($\log Z$), the atmospheric C/O and the pressure of a grey cloud deck ($\log P_{\text{cloud}}$). The metallicity is defined relative to solar (Asplund et al. 2009) and PLATON’s default C/O ratio is 0.53. We place wide flat priors on each parameter of $1.20 < R_p < 1.47 R_J$, $300 < T_{\text{iso}} < 2500$ K, $-1 < \log Z < 3$, $0.05 < \text{C/O} < 2.0$, and $-1 < \log P_{\text{cloud}} < 5$ Pa. We fixed the stellar radius to $1.477 R_\odot$ and planet mass to $0.542 M_J$ (Bonomo et al. 2017). We explored the parameter space using nested sampling, implemented through DYNesty (Speagle 2020), with 1000 live points. We ran these retrievals for both the Tiberius and Eureka! spectra at $R = 100$ and $R = 400$. The posterior medians, 16th and 84th percentiles are given for each fit parameter in Table E1 with the best-fitting models plotted in Figure 10.

As shown in Table E1, our PLATON analysis favours super-solar metallicities of $> 29\times$ solar and $> 38\times$ solar to 1σ for Tiberius and Eureka!, respectively. The median retrieved C/O for both reductions of the data are consistent with solar albeit with relatively large uncertainties (C/O = $0.45^{+0.18}_{-0.20}$ and $0.54^{+0.15}_{-0.21}$ for Tiberius and Eureka!, respectively). However, as we showed in Section 4, our interior structure models place a 2σ upper limit on WASP-15b’s metal mass fraction of 0.36. If we exclude the retrieval samples with

metal mass fractions greater than this and recalculate our posteriors, we find a revised metallicity constraint of 35^{+23}_{-19} and $41^{+21}_{-22}\times$ solar for Tiberius and Eureka!, respectively, while C/O does not change significantly (Table E1). We consider these to be a more accurate inference of WASP-15b’s true atmospheric metallicity. Figure 10 shows the corner plot after excluding the unphysically high metallicity solutions. Figure E3 shows the corner plot over the full metallicity range.

Table E1 demonstrates that our inferences with PLATON are insensitive to whether we run our retrievals on the $R = 100$ or $R = 400$ spectra. For this reason, we only plot the results from our $R = 100$ retrievals (Figure 10).

In summary, all of our retrieval analyses converge to a super-solar metallicity with a C/O consistent with solar. For PLATON and BeAR, the loose metallicity prior allows for unphysically high metallicities which we exclude based on interior structure models of WASP-15b (Section 4). We discuss the comparison between the retrievals in more detail in Section 8.1.

6 INTERPRETING THE SPECTRUM WITH A 3D GENERAL CIRCULATION MODEL

To investigate the potential impact of spatial inhomogeneities in WASP-15b’s atmosphere on the observed transmission spectrum, we performed simulations of WASP-15b’s atmosphere using the Met Office Unified Model (UM), which is a 3D climate model of a planetary atmosphere (also known as a general circulation model, or a GCM). We used the same basic UM setup as in Drummond et al. (2020), Zamyatina et al. (2023) and Zamyatina et al. (2024) that provides the coupling between the dynamics, radiative transfer and chemistry. In brief, UM’s dynamical core (ENDGame, Wood et al. 2014; Mayne et al. 2014a,b) solves the full, deep-atmosphere, non-hydrostatic equations of motion on a constant angular grid using a semi-implicit semi-Lagrangian scheme. The UM’s radiative transfer component (SOCRATES, Edwards 1996; Edwards & Slingo 1996; Amundsen et al. 2014, 2016, 2017) solves the two-stream equations and treats opacities using the correlated- k and equivalent extinction methods. Opacity sources considered in the radiative transfer include the absorption due to H_2O , CO , CO_2 , CH_4 , NH_3 , HCN , Li , Na , K , Rb , Cs and collision-induced absorption due to H_2 - H_2 and H_2 - He as well as Rayleigh scattering due to H_2 and He (for the line list information, see Goyal et al. 2020). Lastly, the UM’s chemistry component provides several chemical schemes for simulating the evolution of hot-Jupiter gas-phase chemistry, with the “equilibrium” and “kinetics” chemical schemes used in this study and described below. We chose a model grid resolution of 2.5° in longitude by 2° in latitude and 86 vertical levels equally spaced in height (covering pressures from ~ 200 bar to $\sim 10^{-5}$ bar). This grid resolution is too coarse to resolve convection; however, we do not find that a convective adjustment or a similar correction is required. Even so, a longitudinal filter is used to maintain numerical stability, with the filtering constant of the horizontal wind, K , equal to 0.04 (see Mayne et al. 2014a,b; Christie et al. 2024). For the stellar spectrum we used a PHOENIX BT-Settl model (Rajpurohit et al. 2013) with parameters from Table F1, and for the planet — parameters from Table F2.

We performed two simulations. One simulation (which we refer to as the UM “equilibrium” simulation), used a chemical equilibrium scheme to compute the change in chemical species abundances induced by the changes in atmospheric pressure and temperature only. The other simulation (which we refer to as the UM “kinetics” simulation), allowed for departures from chemical equilibrium due to

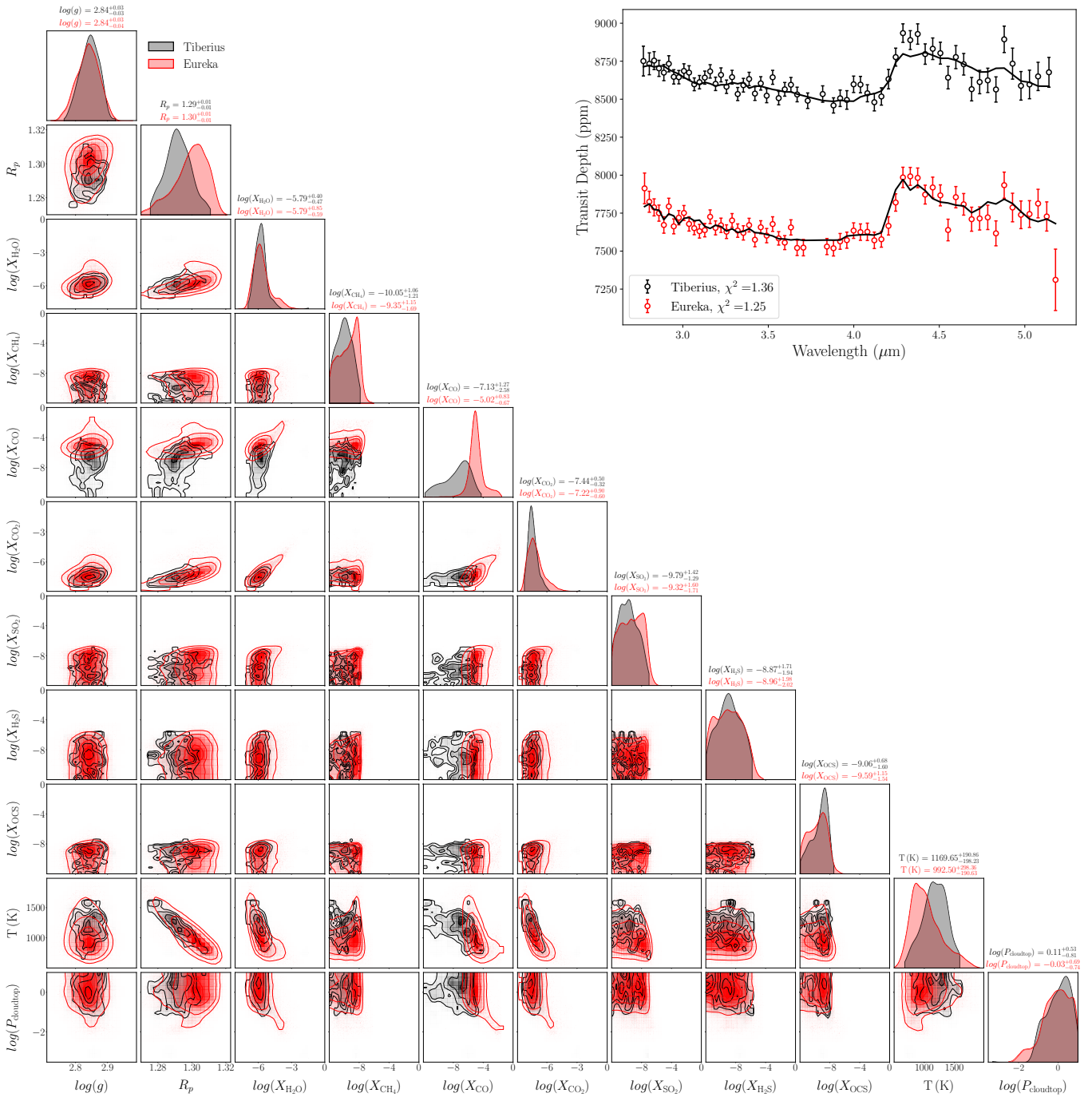


Figure 9. Cornerplot showing the posteriors from the BeAR retrievals on the Tiberius (black) and Eureka! (red) reductions of WASP-15 b at $R = 100$, restricted to the metallicities allowed by the interior structure model. The top right insert shows the best-fit models for the Tiberius (black) and Eureka! (red) reductions. The Eureka! spectrum is offset by 1000 ppm for visualisation purposes. The legend in the bottom left indicates the reduced χ^2 values for each of the fits.

disequilibrium thermochemistry (but omitting photolysis) and used a kinetics chemical scheme to compute the change in chemical species abundances caused not only by the changes in atmospheric pressure and temperature, but also by the changes in the production and loss of these species during their atmospheric transport. Chemical species included in both UM simulations were those present in the Venot et al. (2019) C-O-N-H reduced chemical network. Abundances of alkali metals not included in the Venot et al. (2019) network — Li, Na, K,

Rb and Cs — were calculated using a threshold method outlined in Amundsen et al. (2016). Both UM simulations assumed an aerosol-free atmosphere with $10\times$ solar metallicity and C/O of 0.55 (Asplund et al. 2009). Additional details about the simulations, i.e. initialisation, runtime and the calculation of transmission spectra, are given in Appendix F.

Figure 11 shows the comparison of WASP-15b’s limb-average transmission spectra observed with JWST NIRSpec/G395H and pre-

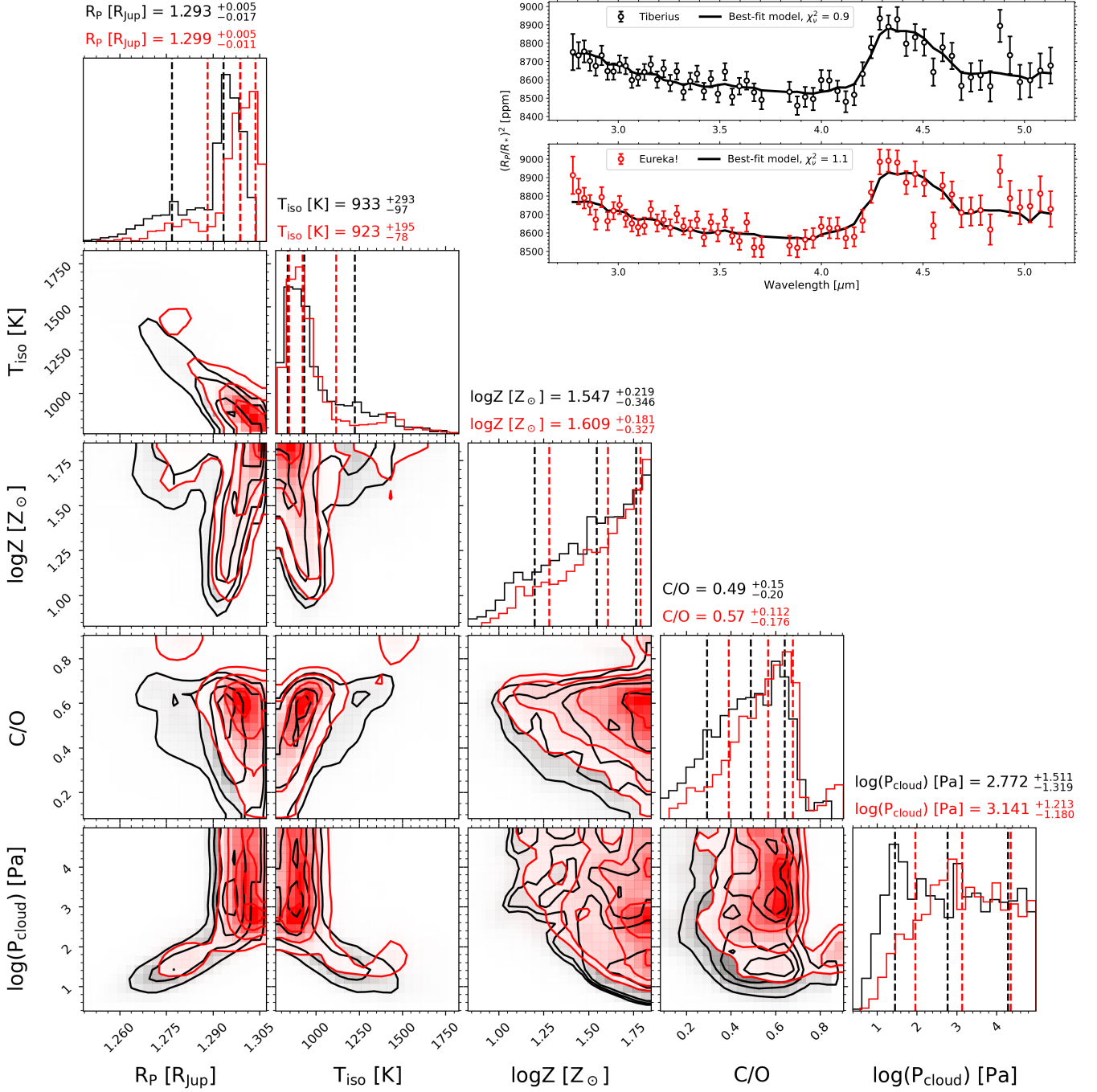


Figure 10. The corner plot and best-fit models from our 1D chemical equilibrium atmosphere retrievals with PLATON run on the $R = 100$ spectra, after excluding the unphysically high metallicity solutions. The black contours correspond to the Tiberius retrieval and the red contours to the Eureka! retrieval. The vertical dashed lines indicate the 16th, 50th (median) and 84th percentiles, which are also given in the axes titles.

dictated by the UM. For the purpose of this comparison, the UM spectra were fitted to the results from the Tiberius reduction at $R = 100$ using a least squares fit, with the required-for-fitting vertical offsets needing to be -1523 ppm and -1515 ppm for the equilibrium and kinetics simulations, respectively. The results from the Eureka! reduction are presented alongside those from Tiberius but are not used for fitting. Overall, this comparison demonstrates that the UM simulations predict the general shape of WASP-15b’s limb-average

transmission spectrum rather well. Both simulations suggest that H_2O , CO and CO_2 are the major contributors to WASP-15b’s opacity at the limbs. The enhancements in the observed transit depths at wavelengths where SO_2 and OCS absorb are not captured by the UM due to the lack of sulphur chemistry in the model.

Our GCM simulations suggest that the constraints on H_2O and CO_2 abundances, and by extension, on C/O, derived from JWST NIR-Spec/G395H transit observations of planets like WASP-15b, could

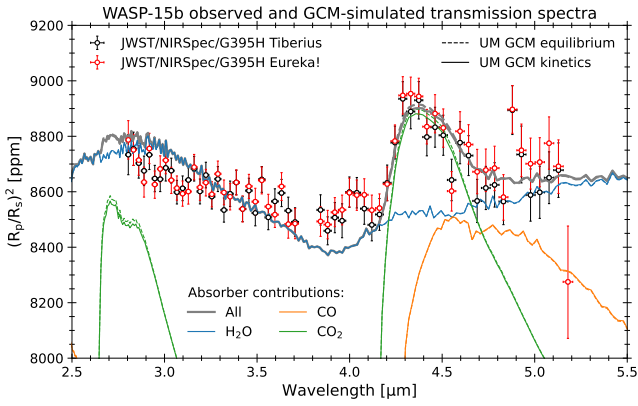


Figure 11. WASP-15b’s $R = 100$ limb-averaged transmission spectra obtained using the Tiberius (black points) and Eureka! (red points) reductions compared to the spectra predicted by the UM equilibrium (dashed lines) and kinetics (solid lines) simulations. UM simulations suggest that H_2O (blue lines), CO (orange lines) and CO_2 (green lines) are the major contributors to the observed limb-averaged transmission spectrum.

be informative not only in the context of the limbs of such planets but also in the context of their entire photospheres. To corroborate that we show the vertical profiles of major C- and O-bearing radiatively active species, CH_4 , CO , CO_2 , H_2O and HCN (and NH_3 for completeness) predicted by the equilibrium and kinetics simulations in Figure 12. Firstly, we see that transport-induced quenching, a process capable of altering C and O budget and distribution at observable pressures in transmission (see Moses 2014, for review), causes CH_4 , HCN and NH_3 profiles in the kinetics simulation to diverge from those at chemical equilibrium: CH_4 is depleted while HCN and NH_3 abundances are enhanced at pressures lower than $\sim 10^{-1}$ bar. However, these disequilibrium changes in CH_4 and NH_3 would not cause the contributions of CH_4 and HCN to the overall absorption by C-bearing species in WASP-15b’s photosphere to be much different from their contributions at chemical equilibrium, because *both* simulations predict that abundances of CH_4 and HCN are low (lower than 1 ppm) throughout the entire GCM model domain. Meanwhile, H_2O , CO and CO_2 are more abundant than CH_4 and HCN in *both* simulations: H_2O and CO reach $\sim 10,000$ ppm and CO_2 ~ 10 ppm. H_2O , CO and CO_2 are also rather uniformly distributed throughout the GCM model domain. Together, low CH_4 and HCN abundances but high H_2O , CO and CO_2 abundances and their uniform spatial distribution, imply that H_2O , CO and CO_2 would (1) account for the majority of C and O in WASP-15b’s photosphere and (2) their contribution to the opacity at the limbs of the planet would be representative of their contribution to the opacity across the entire planet’s photosphere.

7 PHOTOCHEMICAL MODELLING

The evidence for absorption by SO_2 indicates that photochemistry is an active process in the atmosphere of WASP-15b. We model the photochemical processes in this atmosphere using VULCAN, a 1D kinetics model that treats photochemical (Tsai et al. 2021) and thermochemical (Tsai et al. 2017) reactions. The VULCAN setup used in this work solves the Eulerian continuity equations, including chemical sources/sinks and diffusive transport. We use the updated

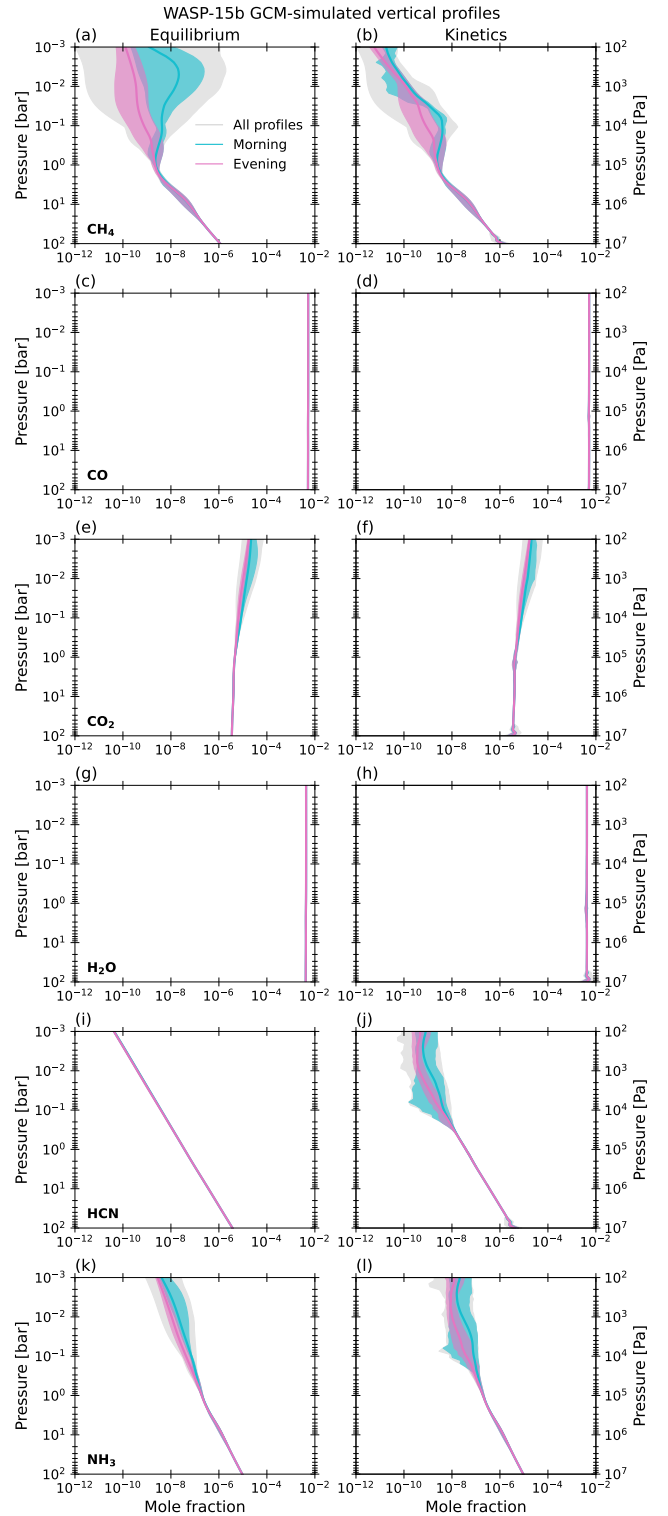


Figure 12. CH_4 , CO , CO_2 , H_2O , HCN and NH_3 vertical profiles predicted by the UM equilibrium (left column) and kinetics (right column) simulations of WASP-15b’s atmosphere. Grey shading shows the range of abundances for the entire atmosphere, cyan shading — for the morning terminator only, pink shading — for the evening terminator only. Solid cyan and pink lines indicate the meridional mean for the morning and evening terminator, respectively.

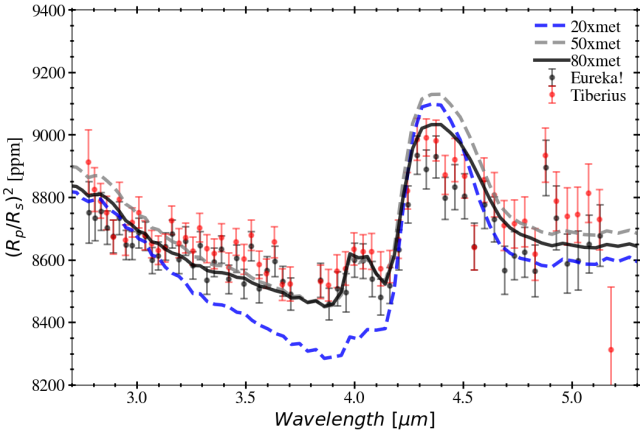


Figure 13. Photochemical model spectra for WASP-15b at 80× (solid, black), 50× (dashed, gray), and 20× (dashed, blue) solar metallicities as compared to the Tiberius (black points) and Eureka! (red points) reductions. Photochemical models suggest that the observed SO₂ feature is indicative of a high metallicity atmosphere.

C-H-N-O-S network³ for hydrogen-dominated atmospheres that importantly considers S-bearing species.

We consider a grid of models based on the temperature profiles at the terminators of WASP-15b as calculated in the equilibrium UM GCM described in Section 6 and shown in Section G1. We use a K_{zz} profile based on the scaling relations in Moses et al. (2022) using an internal temperature of $T_{\text{int}} = 100$ K. We use a host star stellar spectrum for a 6500 K star from the stellar spectral grid in Rugheimer et al. (2013), which combines synthetic ATLAS spectra (Kurucz 1979) with observed spectra from the International Ultraviolet Explorer for wavelengths less than 300 nm. We do not consider the impact of aerosol opacity in our models. The grid spans a range of planet metallicities from 10 × solar, consistent with the input UM GCM, to 100 × solar in intervals of 10. By extending to metallicities higher than those considered by our GCM model, we made the modelling trade-off of considering the differences in photochemistry on the terminators of WASP-15b based on the GCM modelling in-lieu of more self-consistent atmospheric modelling. To create spectra from the photochemical models, we use the PICASO radiative transfer code (Batalha et al. 2019) with a resolution of $R = 100$. The molecular opacities used to generate the transmission spectra in this work are taken from the references in Section G2.

Our models indicate that WASP-15b is likely to be substantially enhanced in metallicity compared to solar to reproduce the observed SO₂ feature, as shown in Figure 13. To reproduce the amplitudes of all of the observed features, namely SO₂, H₂O, and CO₂, a metallicity of either ~ 80× solar or greater is preferred. We emphasise that the high metallicity required to reproduce the spectrum with photochemical modelling is driven by both the SO₂ and CO₂ feature amplitude (and to a lesser extent the H₂O feature amplitude as demonstrated in Section 5). Figure 14 (top panel) shows how the amplitude of the SO₂ feature changes with metallicity as compared to the amplitude of the observed SO₂ feature. The abundance of SO₂ is highly sensitive to metallicity due to the net chemical reaction network that produces SO₂ which requires two H₂O molecules to interact with every H₂S

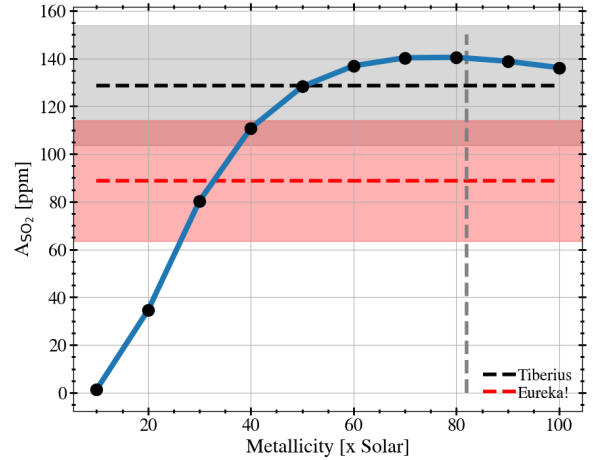
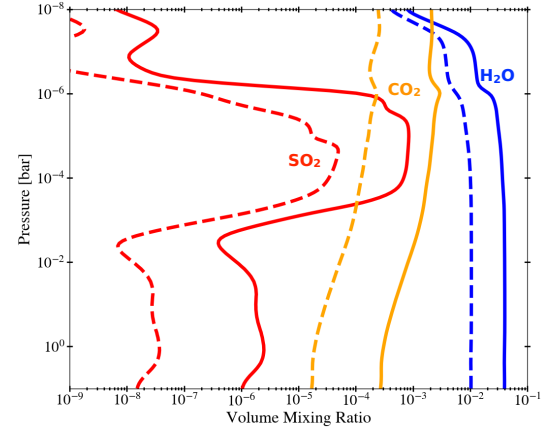


Figure 14. Top: The vertical distribution of SO₂, CO₂, and H₂O as predicted by the VULCAN photochemical model for an atmosphere with 80× solar metallicity (solid lines) and 20× solar metallicity (dashed lines). All three key species have abundances that change substantially with increased metallicity. Bottom: The predicted amplitude of the 4.05 μm feature (A_{SO_2}) varies by more than 100 ppm as a function of atmospheric metallicity. The observed amplitude and uncertainty of the feature are shown by the horizontal dashed lines and shaded regions for Tiberius (grey) and Eureka! (red). This indicates a substantially metal-rich atmosphere based on our photochemical modelling. The vertical dashed grey line indicates the upper limit on the atmospheric metallicity derived from the interior structure model (Section 4).

molecule (Tsai et al. 2023; Powell et al. 2024). This effect can be seen in our model grid in Figure 14 (bottom panel) where we find that the peak SO₂ abundance increases by more than an order of magnitude for substantially metal-rich atmospheres (e.g., 80× solar) as compared to more moderately enriched atmospheres (e.g., 20× solar). We note that while both reductions are consistent with SO₂ amplitudes produced from models with lower metallicities than our nominal case, the CO₂ amplitude is systematically higher than our best-fit 80x metallicity case for those lower metallicity models (e.g., Figure 13).

The photochemical modelling results thus point towards a very high metallicity atmosphere for WASP-15b if the elements vary according to a solar abundance. Our best-fit metallicity (80× solar) indicates that WASP-15b may have a metallicity near the maximum metallicity inferred from interior structure models (82× solar, Section 4). Future work that varies the individual abundance ratios of the different atomic species will be useful to better understand the chemistry of WASP-15b’s atmosphere.

³ https://github.com/exoclime/VULCAN/blob/master/thermo/SNCHO_photo_network_2024.txt

8 DISCUSSION

8.1 Differences between reductions and retrievals

Above, we presented inferences regarding WASP-15b’s atmosphere from two different data reduction pipelines (Section 3) and three different retrieval models (Section 5). While all approaches are consistent with super-solar metallicity atmospheres and solar C/O, the retrieved values do differ (Table E1). These differences appear to be more driven by the retrieval model than the reduction pipeline. This is evidenced by the fact that the retrieval codes are largely insensitive to the input spectrum (Tiberius vs Eureka!), with the greater differences arising between retrieval codes. However, these differences are reduced when we exclude the unphysically high metallicity solutions from the BeAR and PLATON retrievals.

When comparing the results between retrieval codes, it is important to consider how each code defines its parameters. For example, `petitRADTRANS`’s chemical equilibrium models parameterise metallicity as [Fe/H] with chemical equilibrium grids calculated over a range of [Fe/H]. However, when adjusting the C and O abundances, `petitRADTRANS` scales C/H with metallicity and then sets O/H according to C/O. PLATON takes the opposite approach, adjusting O/H based on metallicity, Z ([M/H]), and then setting C/H based on C/O. The approach of both `petitRADTRANS` and PLATON means that (C+O)/H does not respect scaled metallicity abundances.

Furthermore, in our `petitRADTRANS` retrievals, we included the planet’s surface gravity as a free parameter with a Gaussian prior. PLATON does not include the surface gravity as a fit parameter, instead allowing the planet mass to be a fit parameter (in addition to the planet radius). In our PLATON retrievals, we fix the planet’s mass and only fit for the radius. In a further test, we ran a retrieval with mass as a fit parameter with a Gaussian prior from [Bonomo et al. \(2017\)](#) but found this made no difference to our resulting posteriors. With regard to the cloud-top pressure, PLATON recovers a lower pressure cloud deck than `petitRADTRANS`, albeit with large uncertainties. However, this is misleading as the PLATON corner plot (Figure 10) shows that the cloud-top pressure is actually unconstrained with a lower limit of ≥ 10 Pa (0.1 mbar). It is important to note that the reference pressure is fixed to 1 mbar in our `petitRADTRANS` retrievals and to 1 bar in our PLATON retrievals.

Of the different `petitRADTRANS` setups, we favour the ‘hybrid chemistry’ retrievals owing to their better fits to the data (Figure 7). These follow equilibrium chemistry, but with the addition of free abundances for SO₂ and OCS. However, all `petitRADTRANS` approaches produce consistent results (Table E1).

From our retrievals, the isothermal temperatures converge to temperatures that are 600–700 K cooler than the equilibrium temperature of the planet (1676 ± 29 K), albeit with large uncertainties. Retrieved temperatures are often cooler than the equilibrium temperatures due in part to the assumption of 1D atmospheres ([MacDonald et al. 2020](#)).

8.2 WASP-15b’s atmospheric composition and predictions from migration scenarios

Despite the differences in abundances retrieved by each code (Table E1), they consistently point towards a super solar metallicity and an approximately solar C/O ratio. Our GCM simulations (Section 6), that included C-O-N-H gas-phase chemistry and assumed aerosol-free conditions, suggest that CO, H₂O and CO₂ are the most abundant C- and O-bearing chemical species in WASP-15b’s atmosphere. This supports our use of NIRSpc/G395H to measure the planet’s C/O from its H₂O and CO₂ features. Given that these GCM simulations

also predict that the spatial distribution of CO, H₂O and CO₂ is rather uniform throughout the entire GCM model domain (with CO₂ variations in the vertical being less than an order of magnitude, Figure 12), this suggests that CO, H₂O and CO₂’s contribution to the opacity at the limbs of the planet is representative of their contribution to the opacity across the entire planet’s photosphere.

As explained in the introduction, WASP-15b is part of our ongoing survey ([Kirk et al. 2024a](#)) to determine whether aligned and misaligned hot Jupiters around F stars have different C/O ratios and metallicities based on their likely different migration mechanisms (disc vs. disc-free/high-eccentricity).

WASP-15b is a misaligned hot Jupiter ($\lambda = -139.6_{-5.2}^{+4.3}$, [Triaud et al. 2010](#)), which suggests it underwent disc-free (high-eccentricity) migration. The super-solar metallicity we infer for WASP-15b indicates the late accretion of planetesimals, which would serve to drive up the O/H of its atmosphere ([Booth et al. 2017](#); [Schneider & Bitsch 2021](#)). The fact that we also see evidence for sulphur content (Section 8.3), may additionally point to planetesimal accretion. This is because sulphur in the disc is bound in solids even at high temperatures and therefore cannot be delivered by metal-rich gas accretion in the inner disc ([Bitsch et al. 2022](#)). Given the mass of WASP-15b is much larger than the pebble isolation mass, it likely only had minor pebble accretion late in its formation, instead implying planetesimal accretion as the main driver of solid enrichment.

As shown in [Penzlin & Booth et al. 2024](#), we can determine the relative importance of silicates and carbon grains in setting the atmospheric C/O by comparing WASP-15b’s C/O to the aligned planets in our sample. This is one of the main goals of our observational programme ([Kirk et al. 2024a](#)).

8.3 Sulphur chemistry in WASP-15b’s atmosphere

As described in Sections 5.2 and 7, the absorption features we see at 4.0 and 4.9 μm can be fit with SO₂ and OCS, respectively. We discuss the plausibility of this sulphur chemistry below.

Firstly, we compared WASP-15b to the ERS observations of WASP-39b which resulted in the first detection of SO₂ in an exoplanet’s atmosphere ([Alderson et al. 2023](#); [Rustamkulov et al. 2023](#); [Tsai et al. 2023](#)). The abundance of SO₂ seen in WASP-39b’s spectrum was several orders of magnitude higher than expectations based on equilibrium chemistry. This implies that photochemistry is responsible for the observed abundance of SO₂, with the reaction chain beginning with the photodissociation of water in the planet’s atmosphere ([Tsai et al. 2023](#)). This is why our equilibrium chemistry models, that do not include photochemistry, do not attempt to fit the 4.0 μm feature in WASP-15b’s spectrum (Figures 6, 7, 10 and 11). Given that WASP-15b orbits an earlier spectral type star than WASP-39b (F7, [Triaud et al. 2010](#), vs. G8, [Faedi et al. 2011](#)), and is more irradiated ($T_{\text{eq}} = 1676 \pm 29$ K, [Southworth et al. 2013](#), vs. $T_{\text{eq}} = 1116_{-32}^{+33}$ K, [Faedi et al. 2011](#)), it is likely that photochemistry is also important for its atmosphere.

To determine the amplitude of SO₂ absorption in WASP-15b’s atmosphere relative to WASP-39b, we plot the NIRSpc/G395H transmission spectrum of WASP-39b from [Alderson et al. \(2023\)](#) along with WASP-15b’s transmission spectrum in Figure 15. For this comparison, we binned the WASP-39b spectrum to $R = 100$ and then scaled the transit depths of both WASP-39b and WASP-15b by the transit depth corresponding to one scale height for both planets (421 ppm for WASP-39b and 139 ppm for WASP-15b). This figure indicates that the amplitude of the SO₂ absorption in both planets is approximately one atmospheric scale height. For WASP-39b, the

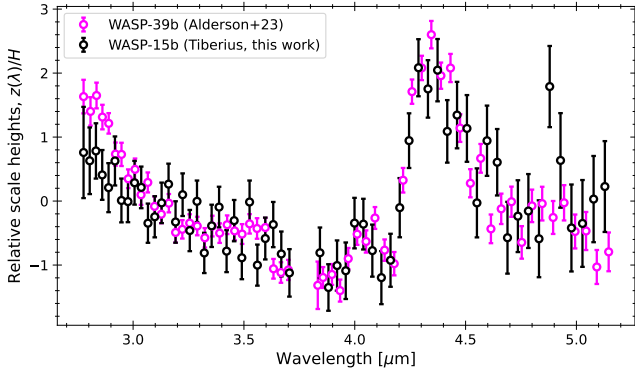


Figure 15. The transmission spectrum of WASP-15b (black, this work) as compared with that of WASP-39b (magenta, Alderson et al. 2023) binned to $R = 100$. The transmission spectra have been scaled with respect to the planets’ atmospheric scale heights.

smaller spectral uncertainties, resulting from the planet’s larger scale height, led to a 4.8σ detection of SO_2 while our larger uncertainties for WASP-15b prevent a statistically significant detection. Follow-up observations of WASP-15b would improve the spectral precision and could search for additional SO_2 absorption features in the mid-infrared (Powell et al. 2024).

The most notable difference between the two planets’ spectra is the feature at $4.9\ \mu\text{m}$ which is only present in WASP-15b’s spectrum. This absorption feature appears in both the Tiberius and Eureka! spectra at $R = 100$ and $R = 400$ (Figure 4). The feature is confined to a single bin (= 61 pixels) at $R = 100$ and a handful of bins in the $R = 400$ spectrum. By fitting a Gaussian to the $R = 400$ transmission spectrum at these wavelengths, we determine that this feature has a central wavelength of $4.90\ \mu\text{m}$ and a full width at half maximum of $0.05\ \mu\text{m}$.

We investigated whether this feature is correlated to any unusual behaviour in limb darkening, systematics coefficients, excess red and white noise, and excess bad pixels at these wavelengths. We found no correlation between any of these parameters and the outliers at these wavelengths. Given these tests, and the fact that the absorption feature is independently seen in both the Tiberius and Eureka! reductions, we conclude that this is a real absorption feature.

To interpret what may be the cause of this feature, we explored a number of different molecules that would be present in both chemical equilibrium and disequilibrium, including CH_4 , CO , H_2S , HCN , O_3 , PH_3 , NH_3 , C_2H_2 , SO_2 , NO , HC_3N , H_2CO , CS_2 , SO , SH , OCS , OH , AlH , AlO , CaH , CrH , FeH , MgH , MgO , NaH , SiO , and SiO_2 . Of these molecules, the only ones that matched the wavelength of the feature we see are OCS (carbonyl sulphide) and O_3 (ozone). We ruled out O_3 based on the feature width (O_3 would result in a much broader feature) and the implausibility of finding the large abundances of O_3 necessary to match the feature strength in a H_2 -dominated atmosphere.

In Figure 7 we showed how the inclusion of OCS in our free and hybrid retrievals with `petitRADTRANS` leads to a better fit of the $4.9\ \mu\text{m}$ absorption feature. However, this figure also showed that the width of the feature at $4.9\ \mu\text{m}$ is narrower than expected for OCS . We investigated if the narrowness of the feature could be caused by OCS at lower pressures or temperatures than the bulk atmospheric composition responsible for the other spectral features. To do this we ran the `petitRADTRANS` forward model with an abundance of OCS localised between 1 and $100\ \mu\text{bar}$, and attempted to vary the

temperature and OCS abundance in this part of the atmosphere to fit the feature. A temperature of 300 K with a 2% OCS mixing ratio in this part of the atmosphere gave a feature that was still slightly broader and weaker than the feature observed in the $R = 400$ spectrum. Such a cold temperature and high abundance of OCS localised to the upper part of the atmosphere of WASP-15b is highly unphysical.

Aside from the quality of the fits, there are caveats regarding the physics of the OCS interpretation, namely that OCS is not expected to be abundant at the low pressures (\lesssim mbar) probed by transmission (Tsai et al. 2021, 2023). Similar to H_2S , OCS is destroyed by photodissociation as well as by photochemically produced atomic H and atomic S. To have OCS at the high altitudes we are observing, either the photochemical sinks must be suppressed, or there exist unidentified production mechanisms. Jordan et al. (2021) found that OCS can survive at high altitudes in a Venus-like atmosphere around M stars with significantly lower NUV flux. However, OCS is expected to be depleted around F-type stars like WASP-15 or even stars with solar-like UV radiation. Alternatively, it is conceivable that OCS might be produced through the oxidation of CS or CS_2 after their formation in the upper atmosphere, although the abundances of CS and CS_2 remain low in our models. The identification of plausible OCS production is beyond the scope of this study.

In summary, we believe that the absorption we see at $4.9\ \mu\text{m}$ is astrophysical and not an instrumental artefact. While OCS is the leading candidate, there are several caveats to this interpretation. Alternatively, the feature observed at $4.9\ \mu\text{m}$ could be produced by a molecule not included in currently available line lists, necessitating additional laboratory work (Fortney et al. 2019).

9 CONCLUSIONS

We present the $2.8\text{--}5.2\ \mu\text{m}$ transmission spectrum of the misaligned hot Jupiter WASP-15b obtained from a single transit observation with JWST/NIRSpec/G395H. We reduce our data with three independent approaches and find minimal red noise in our data, likely due to the quiet and relatively faint star which allows for a high number groups per integration (44). This allows us to measure a precise transmission spectrum (median uncertainty of 55 ppm at $R = 100$ and 106 ppm at $R = 400$).

We interpret WASP-15b’s spectrum using three independent retrieval codes and GCM simulations. Our spectrum reveals significant absorption from H_2O (4.9σ) and CO_2 (8.9σ), with evidence for SO_2 and absorption at $4.9\ \mu\text{m}$ for which the current best candidate is OCS , albeit with several caveats. If further observations of this planet are able to confirm if the feature at $4.9\ \mu\text{m}$ is indeed OCS this would be the first detection of this molecule in an exoplanet atmosphere and would allow for new tests of sulphur chemistry in exoplanet atmospheres.

Despite some differences between the absolute abundances inferred from which reduction and retrieval code is adopted, all methods converge on a super-solar metallicity atmosphere ($\gtrsim 15\times$ solar) and a C/O that is consistent with solar but with relatively large uncertainties. Our GCM simulations for WASP-15b suggest that the C/O we measure at the limb is likely representative of the entire photosphere due to the mostly uniform spatial distribution of H_2O , CO_2 and CO .

The super-solar metallicity we infer for WASP-15b indicates the late accretion of planetesimals. The fact that we also see evidence for sulphur content, may additionally point to planetesimal accretion as sulphur cannot be delivered by metal-rich gas accretion in the inner disc (Bitsch et al. 2022). Given the mass of WASP-15b is

much larger than the pebble isolation mass, it likely only had minor pebble accretion late in its formation, instead implying planetesimal accretion as the main driver of solid enrichment. However, we refrain from making comparisons between the planet's C/O and formation models, such as those of [Penzlin & Booth et al. 2024](#), until we have analysed the rest of the planets in our programme ([Kirk et al. 2024a](#)), as these comparisons need to be performed for a sample of planets rather than individual objects.

This is the first planet to be observed as part of our BOWIE-ALIGN programme that seeks to determine whether a hot Jupiter's atmospheric composition depends on its method of migration, as indicated by its obliquity around an F star (GO 3838, PIs: Kirk & Ahler, [Kirk et al. 2024a](#)). By combining WASP-15b with the results from the rest of our programme, we will test models of planet formation and demonstrate whether atmospheric composition can be reliably traced to formation history.

ACKNOWLEDGEMENTS

This work is based on observations made with the NASA/ESA/CSA James Webb Space Telescope. The data were obtained from the Mikulski Archive for Space Telescopes at the Space Telescope Science Institute, which is operated by the Association of Universities for Research in Astronomy, Inc., under NASA contract NAS 5-03127 for JWST. These observations are associated with program #3838. This work was inspired by collaboration through the UK-led BOWIE+ collaboration. JK acknowledges financial support from Imperial College London through an Imperial College Research Fellowship grant. N.J.M., D.E.S. and M.Z. acknowledge support from a UKRI Future Leaders Fellowship [Grant MR/T040866/1], a Science and Technology Facilities Funding Council Nucleus Award [Grant ST/T000082/1], and the Leverhulme Trust through a research project grant [RPG-2020-82]. RAB thanks the Royal Society for their support through a University Research Fellowship. PJW acknowledges support from STFC through consolidated grant ST/X001121/1. VP acknowledges support from the UKRI Future Leaders Fellowship grant MR/S035214/1 and UKRI Science and Technology Facilities Council (STFC) through the consolidated grant ST/X001121/1.

DATA AVAILABILITY

We will make our data products available on Zenodo upon acceptance of the manuscript. We describe the data products resulting from our survey in [Kirk et al. \(2024a\)](#).

REFERENCES

Abel M., Frommhold L., Li X., Hunt K. L. C., 2011, *The Journal of Physical Chemistry A*, 115, 6805
 Abel M., Frommhold L., Li X., Hunt K. L. C., 2012, *The Journal of Chemical Physics*, 136, 044319
 Ahler E.-M., et al., 2023, *Nature*, 614, 653
 Albrecht S., et al., 2012, *ApJ*, 757, 18
 Alderson L., et al., 2023, *Nature*, 614, 664
 Amundsen D. S., Baraffe I., Tremblin P., Manners J., Hayek W., Mayne N. J., Acreman D. M., 2014, *Astronomy & Astrophysics*, 564, 1
 Amundsen D. S., et al., 2016, *Astronomy & Astrophysics*, 595, A36
 Amundsen D. S., Tremblin P., Manners J., Baraffe I., Mayne N. J., 2017, *Astronomy & Astrophysics*, 598, 1
 Asplund M., Grevesse N., Sauval A. J., Scott P., 2009, *ARA&A*, 47, 481

Azzam A. A., Tennyson J., Yurchenko S. N., Naumenko O. V., 2016a, *Monthly Notices of the Royal Astronomical Society*, 460, 4063
 Azzam A. A., Tennyson J., Yurchenko S. N., Naumenko O. V., 2016b, *Monthly Notices of the Royal Astronomical Society*, 460, 4063
 Barber R., Strange J., Hill C., Polyansky O., Mellau G. C., Yurchenko S., Tennyson J., 2014, *Monthly Notices of the Royal Astronomical Society*, 437, 1828
 Batalha N. E., Marley M. S., Lewis N. K., Fortney J. J., 2019, *ApJ*, 878, 70
 Bell T. J., et al., 2022, *JOSS*, 7, 4503
 Benneke B., Seager S., 2013, *The Astrophysical Journal*, 778, 153
 Bitsch B., Schneider A. D., Kreidberg L., 2022, *A&A*, 665, A138
 Bonomo A. S., et al., 2017, *A&A*, 602, A107
 Booth R. A., Clarke C. J., Madhusudhan N., Ilee J. D., 2017, *MNRAS*, 469, 3994
 Brady R. P., Yurchenko S. N., Tennyson J., Kim G.-S., 2024, *Monthly Notices of the Royal Astronomical Society*, 527, 6675
 Buchner J., et al., 2014, *Astronomy & Astrophysics*, 564, A125
 Christie D. A., Mayne N. J., Zamyatina M., Baskett H., Evans-Soma T. M., Wood N., Kohary K., 2024, *Monthly Notices of the Royal Astronomical Society*, 532, 3001
 Chubb K. L., et al., 2021, *Astronomy & Astrophysics*, 646, A21
 Claringbold A., Rimmer P., Rugheimer S., Shorttle O., 2023, *The Astronomical Journal*, 166, 39
 Coles P. A., Yurchenko S. N., Tennyson J., 2019, *Monthly Notices of the Royal Astronomical Society*, 490, 4638
 Dobbs-Dixon I., Cowan N. B., 2017, *The Astrophysical Journal*, 851, L26
 Drummond B., et al., 2020, *Astronomy & Astrophysics*, 636, A68
 Edwards J. M., 1996, *Journal of the Atmospheric Sciences*, 53
 Edwards J. M., Slingo A., 1996, *Quarterly Journal of the Royal Meteorological Society*, 122, 689
 Espinoza N., Fortney J. J., Miguel Y., Thorngren D., Murray-Clay R., 2017, *ApJ*, 838, L9
 Faedi F., et al., 2011, *A&A*, 531, A40
 Fairman C., Wakeford H. R., MacDonald R. J., 2024, *AJ*, 167, 240
 Faure A., Wiesenfeld L., Drouin B. J., Tennyson J., 2013, *J. Quant. Spectrosc. Radiative Transfer*, 116, 79
 Feinstein A. D., et al., 2023, *Nature*, 614, 670
 Feroz F., Hobson M. P., 2008, *MNRAS*, 384, 449
 Ford E. B., Rasio F. A., 2008, *ApJ*, 686, 621
 Foreman-Mackey D., Hogg D. W., Lang D., Goodman J., 2013, *PASP*, 125, 306
 Fortney J., et al., 2019, *Astro2020: Decadal Survey on Astronomy and Astrophysics*, 2020, 146
 Gaia Collaboration et al., 2023, *A&A*, 674, A1
 Gordon I. E., Rothman L. S., Tan Y., Kochanov R. V., Hill C., 2017a, in *72nd International Symposium on Molecular Spectroscopy*. p. TJ08, doi:10.15278/isms.2017.TJ08
 Gordon I. E., et al., 2017b, *J. Quant. Spectrosc. Radiative Transfer*, 203, 3
 Goyal J. M., et al., 2020, *Monthly Notices of the Royal Astronomical Society*, 498, 4680
 Grant D., Wakeford H. R., 2024, *Journal of Open Source Software*, 9, 6816
 Helling C., et al., 2016, *MNRAS*, 460, 855
 Huang X., Gamache R. R., Freedman R. S., Schwenke D. W., Lee T. J., 2014, *Journal of Quantitative Spectroscopy and Radiative Transfer*, 147, 134
 JWST Transiting Exoplanet Community Early Release Science Team et al., 2023, *Nature*, 614, 649
 Jakobsen P., et al., 2022, *A&A*, 661, A80
 Jordan S., Rimmer P. B., Shorttle O., Constantinou T., 2021, *ApJ*, 922, 44
 Kipping D. M., Tinetti G., 2010, *MNRAS*, 407, 2589
 Kirk J., Wheatley P. J., Louden T., Doyle A. P., Skillen I., McCormac J., Irwin P. G. J., Karjalainen R., 2017, *MNRAS*, 468, 3907
 Kirk J., et al., 2021, *AJ*, 162, 34
 Kirk J., et al., 2024a, *arXiv e-prints*, p. arXiv:2407.03198
 Kirk J., et al., 2024b, *AJ*, 167, 90
 Kitzmann D., Heng K., Oreshenko M., Grimm S. L., Apai D., Bowler B. P., Burgasser A. J., Marley M. S., 2020, *ApJ*, 890, 174
 Kreidberg L., 2015, *PASP*, 127, 1161
 Kurucz R. L., 1979, *ApJS*, 40, 1

Law C. J., et al., 2021, *ApJS*, 257, 3

Lenzuni P., Chernoff D. F., Salpeter E. E., 1991, *ApJS*, 76, 759

Li G., Gordon I. E., Rothman L. S., Tan Y., Hu S.-M., Kassi S., Campargue A., Medvedev E. S., 2015a, *ApJS*, 216, 15

Li G., Gordon I. E., Rothman L. S., Tan Y., Hu S.-M., Kassi S., Campargue A., Medvedev E. S., 2015b, *ApJS*, 216, 15

Lightkurve Collaboration et al., 2018, Lightkurve: Kepler and TESS time series analysis in Python, *Astrophysics Source Code Library* (ascl:1812.013)

Lines S., et al., 2018, *Monthly Notices of the Royal Astronomical Society*, 481, 194

MacDonald R. J., Goyal J. M., Lewis N. K., 2020, *ApJ*, 893, L43

Madhusudhan N., Amin M. A., Kennedy G. M., 2014, *ApJ*, 794, L12

Magic Z., Chiavassa A., Collet R., Asplund M., 2015, *A&A*, 573, A90

Mayne N. J., Baraffe I., Acreman D. M., Smith C., Wood N., Amundsen D. S., Thuburn J., Jackson D. R., 2014a, *Geoscientific Model Development*, 7, 3059

Mayne N. J., et al., 2014b, *Astronomy & Astrophysics*, 561, A1

Mollière P., van Boekel R., Dullemond C., Henning T., Mordasini C., 2015, *The Astrophysical Journal*, 813, 47

Mollière P., van Boekel R., Bouwman J., Henning T., Lagage P.-O., Min M., 2017, *Astronomy & Astrophysics*, 600, A10

Mollière P., Wardenier J., Van Boekel R., Henning T., Molaverdikhani K., Snellen I., 2019, *Astronomy & Astrophysics*, 627, A67

Moran S. E., et al., 2023, *The Astrophysical Journal Letters*, 948, L11

Morbiddelli A., et al., 2016, *Icarus*, 267, 368

Morello G., Zingales T., Martin-Lagarde M., Gastaud R., Lagage P.-O., 2021, *AJ*, 161, 174

Moses J. I., 2014, *Philosophical Transactions of the Royal Society A: Mathematical, Physical and Engineering Sciences*, 372

Moses J. I., Tremblin P., Venot O., Miguel Y., 2022, *Experimental Astronomy*, 53, 279

Muñoz D. J., Lai D., Liu B., 2016, *MNRAS*, 460, 1086

Müller S., Helled R., 2024, *The Astrophysical Journal*, 967, 7

Nasedkin E., Mollière P., Blain D., 2024, *The Journal of Open Source Software*, 9, 5875

Öberg K. I., Murray-Clay R., Bergin E. A., 2011, *ApJ*, 743, L16

Owen J. E., 2020, *MNRAS*, 495, 3160

Owens A., Yurchenko S. N., Tennyson J., 2024, *Monthly Notices of the Royal Astronomical Society*, 530, 4004

Patel J. A., Espinoza N., 2022, *AJ*, 163, 228

Penzlin A. B. T., et al., 2024, arXiv e-prints, p. arXiv:2407.03199

Polyansky O. L., Kyuberis A. A., Zobov N. F., Tennyson J., Yurchenko S. N., Lodi L., 2018a, *MNRAS*, 480, 2597

Polyansky O. L., Kyuberis A. A., Zobov N. F., Tennyson J., Yurchenko S. N., Lodi L., 2018b, *MNRAS*, 480, 2597

Powell D., et al., 2024, *Nature*, 626, 979

Rajpurohit A. S., Reylé C., Allard F., Homeier D., Schultheis M., Bessell M. S., Robin A. C., 2013, *Astronomy & Astrophysics*, 556, A15

Rasio F. A., Ford E. B., 1996, *Science*, 274, 954

Rothman L. S., et al., 2010a, *Journal of Quantitative Spectroscopy and Radiative Transfer*, 111

Rothman L. S., et al., 2010b, *J. Quant. Spectrosc. Radiative Transfer*, 111, 2139

Rugheimer S., Kaltenegger L., Zsom A., Segura A., Sasselov D., 2013, *Astrobiology*, 13, 251

Rustamkulov Z., et al., 2023, *Nature*, 614, 659

Saumon D., Marley M. S., Abel M., Frommhold L., Freedman R. S., 2012, *ApJ*, 750, 74

Schneider A. D., Bitsch B., 2021, *A&A*, 654, A71

Skilling J., 2004, *Bayesian inference and maximum entropy methods in science and engineering*, 735, 395

Southworth J., et al., 2013, *MNRAS*, 434, 1300

Speagle J. S., 2020, *MNRAS*, 493, 3132

Tashkun S. A., Perevalov V. I., 2011, *J. Quant. Spectrosc. Radiative Transfer*, 112, 1403

Thorngren D. P., Fortney J. J., 2018, *AJ*, 155, 214

Thorngren D., Fortney J. J., 2019, *ApJ*, 874, L31

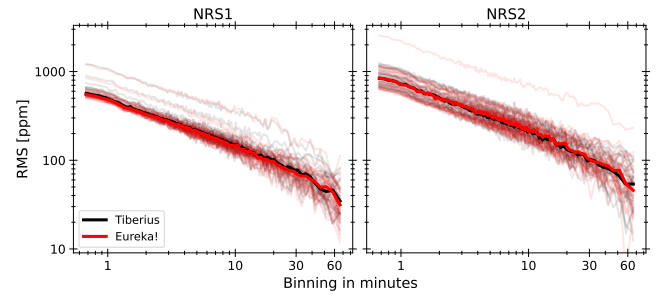


Figure A1. The Allan variance plot from the Tiberius (black) and Eureka! (red) $R = 100$ spectroscopic light curve fits for NRS1 (left panel) and NRS2 (right panel). The thick lines show the median Allan variances.

Thorngren D. P., Fortney J. J., Murray-Clay R. A., Lopez E. D., 2016, *ApJ*, 831, 64

Triaud A. H. M. J., et al., 2010, *A&A*, 524, A25

Trotta R., 2008, *Contemporary Physics*, 49, 71

Tsai S.-M., Lyons J. R., Grosheintz L., Rimmer P. B., Kitzmann D., Heng K., 2017, *ApJS*, 228, 20

Tsai S.-M., Malik M., Kitzmann D., Lyons J. R., Fateev A., Lee E., Heng K., 2021, *ApJ*, 923, 264

Tsai S.-M., et al., 2023, *Nature*, 617, 483

Underwood D. S., Tennyson J., Yurchenko S. N., Huang X., Schwenke D. W., Lee T. J., Clausen S., Fateev A., 2016, *MNRAS*, 459, 3890

Vardya M. S., 1962, *The Astrophysical Journal*, 135, 303

Venot O., Bounaceur R., Dobrijevic M., Hébrard E., Cavalié T., Tremblin P., Drummond B., Charnay B., 2019, *Astronomy & Astrophysics*, 624, A58

Virtanen P., et al., 2020, *Nature Methods*, 17, 261

Wakeford H. R., et al., 2018, *AJ*, 155, 29

West R. G., et al., 2009, *AJ*, 137, 4834

Wilzewski J. S., Gordon I. E., Kochanov R. V., Hill C., Rothman L. S., 2016, *Journal of Quantitative Spectroscopy and Radiative Transfer*, 168, 193

Woitke P., Helling C., Hunter G. H., Millard J. D., Turner G. E., Worters M., Bleic J., Stock J. W., 2018, *A&A*, 614, A1

Wood N., et al., 2014, *Quarterly Journal of the Royal Meteorological Society*, 140, 1505

Wu Y., Murray N., 2003, *ApJ*, 589, 605

Yurchenko S. N., Tennyson J., 2014, *Monthly Notices of the Royal Astronomical Society*, 440, 1649

Yurchenko S. N., Tennyson J., Barber R. J., Thiel W., 2013a, *Journal of Molecular Spectroscopy*, 291, 69

Yurchenko S. N., Tennyson J., Barber R. J., Thiel W., 2013b, *Journal of Molecular Spectroscopy*, 291, 69

Yurchenko S. N., Amundsen D. S., Tennyson J., Waldmann I. P., 2017, *Astronomy & Astrophysics*, 605, A95

Yurchenko S. N., Mellor T. M., Freedman R. S., Tennyson J., 2020, *MNRAS*, 496, 5282

Zamyatina M., et al., 2023, *MNRAS*, 519, 3129

Zamyatina M., et al., 2024, *Monthly Notices of the Royal Astronomical Society*, 529, 1776

Zhang M., Chachan Y., Kempton E. M. R., Knutson H. A., 2019, *PASP*, 131, 034501

Zhang M., Chachan Y., Kempton E. M. R., Knutson H. A., Chang W. H., 2020, *ApJ*, 899, 27

APPENDIX A: ALLAN VARIANCE PLOTS FOR SPECTROSCOPIC LIGHT CURVES

This appendix includes the Allan variance plots for the spectroscopic light curves from both the Tiberius and Eureka! reductions in Figure A1.

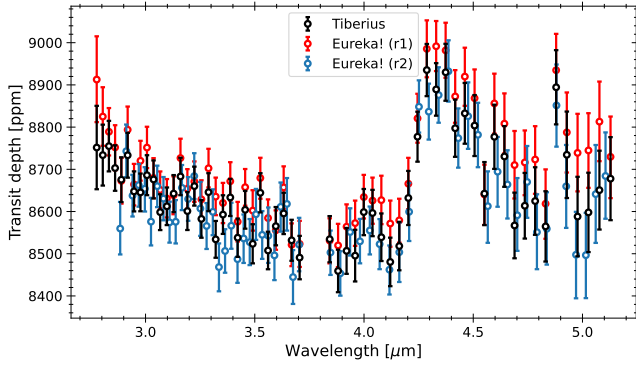


Figure B1. The comparison between the transmission spectra obtained with Tiberius (black), Eureka! reduction 1 (red, Section 3), and Eureka! reduction 2 (blue).

APPENDIX B: SECOND EUREKA! REDUCTION

As mentioned in Section 3, we performed a second, independent reduction with Eureka! to determine how robust our spectrum is to choices made during the spectral extraction process. Aside from a different choice of wavelength binning to generate the spectroscopic light curves, the key difference between this second reduction and the Eureka! reduction presented in Section 3 is that we start with the Stage 1 output of Tiberius as described in Section 3 and use them as inputs to the Stage 2 of Eureka!. We perform the spectral extraction in Eureka!’s Stage 3 the same way as done in Section 3 except we use a $>10\sigma$ threshold for performing the double-iterative masking of outliers along the time axis, extract the background from the area >10 pixels away from central pixel of the trace, and use a full width of 8 pixels for optimal spectral extraction. For the light curve fitting, we followed the same steps in the first reduction as described in Section 3, except we fixed both the quadratic limb-darkening parameters $u1$ and $u2$ to the ExoTiC-LD values.

We present the comparison between the spectra from both Eureka! reductions and the Tiberius reduction in Figure B1. This figure shows that the spectra from each reduction are consistent with one another. Unlike in Figure 4, no transit depth offset has been applied between the spectra in this plot. The differences in the median transit depths are: Eureka! r1 – Tiberius = 38 ppm, Eureka! r2 – Tiberius = –17 ppm (in the overlapping wavelength range, $\geq 2.9\mu\text{m}$). These differences are both less than the median transit depth uncertainties of each spectrum: Eureka! r1 = 54 ppm, Tiberius = 54 ppm, Eureka! r2 = 61 ppm.

APPENDIX C: TESS LIGHT CURVE FITTING

Given the lack of optical wavelength coverage from our G395H transmission spectrum, we decided to fit the TESS light curves. Our goal was to place a constraint on the transit depth at visible wavelengths which could help constrain cloud and haze parameters (e.g., Wakeford et al. 2018; Fairman et al. 2024). Rather than taking the literature TESS transit depth for WASP-15b (Patel & Espinoza 2022), we re-fitted the TESS light curve with the values for the system parameters (T_0 , a/R_* , i) that we derived from our JWST light curves (Tiberius values, Table 1). This was done to avoid a bias in the transit depth arising from inconsistent system parameters.

We used `lightkurve` (Lightkurve Collaboration et al. 2018) to extract the short cadence (SPOC) TESS light curve and phase-folded

this using the period from Patel & Espinoza (2022) and the T_0 from our own JWST light curve fits. We trimmed the phase-folded TESS light curve to have the same out-of-transit baseline as our JWST data and fitted the trimmed light curve using a `batman` model multiplied by a linear polynomial to be consistent with our JWST light curve fits. The resulting R_P/R_* we derive from the TESS light curve is 0.092155 ± 0.000470 ($(R_P/R_*)^2 = 8493 \pm 87$ ppm), which is within 1σ of Patel & Espinoza (2022) but is more precise owing to the fewer free parameters in our model. However, despite this improved precision, the inclusion of the TESS data did not improve the precision of our retrievals and did not substantially change the fit of the GCM spectra to our JWST data, so we opted against using the TESS data in our final analysis.

APPENDIX D: NIGHTSIDE DILUTION CALCULATION

To determine the amplitude of dilution in the transmission spectrum caused by thermal emission from the planet’s nightside, we used both the equations from Kipping & Tinetti (2010) and the ExoTETHyS package (Morello et al. 2021). ExoTETHyS additionally accounts for dilution from the planet’s phase curve variations over the course of a transit observation. Both approaches give consistent results, with the dilution amplitude ranging from 5 ppm at the bluest wavelengths we consider to 14 ppm at the reddest wavelengths. These variations are between 0.06 and $0.2\times$ the uncertainties in our $R = 100$ spectra and so we do not apply a dilution correction to our final transmission spectrum.

APPENDIX E: PARAMETERS AND ADDITIONAL PLOTS FROM ATMOSPHERIC RETRIEVALS

This appendix includes the tabulated parameters from our 1D atmospheric retrievals (Section 5). We also include a `petitRADTRANS` corner plot for the free retrievals (Fig. E1), the `BeAR` $R = 100$ best fit and corner plot without the restricted metallicity (Figure E2) and the `PLATON` corner plot without the restricted metallicity (Figure E3).

Table E1. The results from our retrievals using *petitRADTRANS* (free and equilibrium chemistry, Section 5.2), *BeAR* (free chemistry, Section 5.3) and *PLATON* (equilibrium chemistry, Section 5.4). In this table, the *petitRADTRANS* abundances have been converted from the mass fractions presented in the *petitRADTRANS* corner plots. Both *BeAR* and *PLATON* include additional rows where the posteriors have been recalculated after excluding solutions with $Z > 82\times$ solar, motivated by our interior structure model (Section 4). For the *BeAR* retrievals this is limited to the $R = 100$ case, as removing the high metallicity solutions from the $R = 400$ retrievals does not leave sufficient posterior samples. Parameters that are not fit parameters for each code are marked as "-".

Input spectrum	R_p (R_J)	$\log g$ (cgs)	T_{iso} (K)	$\log P_{\text{cloud}}$ (bar)	Z (\times solar)	C/O	$\log(X_{\text{H}_2\text{O}})$	$\log(X_{\text{CO}_2})$	$\log(X_{\text{CO}})$	$\log(X_{\text{SO}_2})$	$\log(X_{\text{Ocs}})$
<i>petitRADTRANS</i>											
<i>Equilibrium Chemistry:</i>											
Tiberius, $R = 100$	1.302 ± 0.003	2.88 ± 0.05	910^{+110}_{-73}	$-0.50^{+1.61}_{-2.04}$	18^{+22}_{-8}	$0.48^{+0.11}_{-0.16}$	–	–	–	–	–
Eureka!, $R = 100$	1.305 ± 0.002	$2.87^{+0.05}_{-0.04}$	914^{+86}_{-62}	$-0.45^{+1.62}_{-1.76}$	22^{+27}_{-9}	$0.53^{+0.09}_{-0.16}$	–	–	–	–	–
<i>Free Chemistry:</i>											
Tiberius, $R = 100$	1.296 ± 0.013	2.90 ± 0.05	1126^{+239}_{-159}	$-3.19^{+0.81}_{-0.74}$	–	–	$-2.83^{+0.59}_{-0.95}$	$-4.40^{+0.73}_{-1.02}$	$-6.55^{+3.39}_{-3.99}$	$-9.20^{+2.56}_{-2.61}$	$-7.31^{+1.31}_{-3.29}$
Eureka!, $R = 100$	1.304 ± 0.002	$2.90^{+0.05}_{-0.06}$	1081^{+115}_{-137}	$-2.90^{+0.81}_{-0.98}$	–	–	$-3.14^{+0.84}_{-0.82}$	$-4.57^{+1.13}_{-0.95}$	$-3.48^{+1.24}_{-5.51}$	$-8.88^{+2.64}_{-3.02}$	$-6.52^{+1.22}_{-2.64}$
<i>Hybrid Chemistry:</i>											
Tiberius, $R = 100$	1.306 ± 0.002	$2.87^{+0.04}_{-0.05}$	887^{+65}_{-56}	$-0.66^{+1.78}_{-1.83}$	22^{+20}_{-10}	$0.53^{+0.09}_{-0.15}$	–	–	–	$-6.56^{+1.11}_{-4.46}$	$-8.84^{+2.04}_{-3.10}$
Eureka!, $R = 100$	1.303 ± 0.002	2.84 ± 0.05	891^{+47}_{-49}	$-0.48^{+1.68}_{-1.78}$	24^{+19}_{-11}	$0.56^{+0.07}_{-0.13}$	–	–	–	$-5.49^{+0.34}_{-1.63}$	$-6.52^{+0.65}_{-2.15}$
<i>BeAR</i>											
<i>Full prior range:</i>											
Tiberius, $R = 100$	$1.297^{+0.007}_{-0.01}$	2.83 ± 0.03	1031^{+139}_{-128}	$-1.96^{+1.78}_{-1.68}$	–	–	$-0.81^{+0.12}_{-0.16}$	-1.69 ± 0.36	$-7.46^{+3.27}_{-2.72}$	$-7.29^{+2.54}_{-2.72}$	$-4.87^{+1.47}_{-4.09}$
Tiberius, $R = 400$	1.302 ± 0.007	2.84 ± 0.03	1163^{+212}_{-192}	$-1.46^{+1.39}_{-1.38}$	–	–	$-0.82^{+0.15}_{-0.29}$	$-1.13^{+0.23}_{-0.2}$	$-7.59^{+3.2}_{-2.67}$	$-7.99^{+2.28}_{-2.21}$	$-7.69^{+2.3}_{-2.44}$
Eureka!, $R = 100$	$1.301^{+0.008}_{-0.011}$	$2.84^{+0.03}_{-0.04}$	991^{+294}_{-191}	$-0.06^{+0.71}_{-0.78}$	–	–	$-5.77^{+1.0}_{-0.61}$	$-7.18^{+1.08}_{-0.62}$	$-5.01^{+0.91}_{-0.71}$	$-9.28^{+1.62}_{-1.74}$	$-9.52^{+1.19}_{-1.59}$
Eureka!, $R = 400$	$1.296^{+0.01}_{-0.011}$	2.84 ± 0.03	1498^{+274}_{-292}	$-2.09^{+1.58}_{-1.37}$	–	–	$-0.91^{+0.16}_{-0.32}$	$-0.98^{+0.16}_{-0.14}$	$-6.5^{+3.27}_{-3.36}$	$-7.77^{+2.62}_{-2.57}$	$-7.1^{+3.17}_{-2.94}$
<i>High Z solutions excluded</i>											
Tiberius, $R = 100$	1.291 ± 0.007	2.84 ± 0.03	1169^{+190}_{-198}	$0.11^{+0.53}_{-0.81}$	–	–	$-5.79^{+0.4}_{-0.47}$	$-7.44^{+0.5}_{-0.32}$	$-7.13^{+1.27}_{-2.58}$	$-9.79^{+1.42}_{-1.29}$	$-9.06^{+0.68}_{-1.6}$
Eureka!, $R = 100$	$1.301^{+0.008}_{-0.011}$	$2.84^{+0.03}_{-0.04}$	992^{+298}_{-190}	$-0.03^{+0.69}_{-0.74}$	–	–	$-5.79^{+0.85}_{-0.59}$	$-7.22^{+0.9}_{-0.6}$	$-5.02^{+0.83}_{-0.67}$	$-9.32^{+1.6}_{-1.71}$	$-9.59^{+1.15}_{-1.54}$
<i>PLATON</i>											
<i>Full prior range:</i>											
Tiberius, $R = 100$	$1.295^{+0.008}_{-0.013}$	–	1041^{+318}_{-183}	$-3.846^{+1.483}_{-1.382}$	97^{+92}_{-68}	$0.45^{+0.18}_{-0.20}$	–	–	–	–	–
Tiberius, $R = 400$	$1.300^{+0.006}_{-0.008}$	–	1016^{+310}_{-175}	$-2.280^{+1.173}_{-1.391}$	162^{+77}_{-92}	$0.45^{+0.17}_{-0.20}$	–	–	–	–	–
Eureka!, $R = 100$	$1.301^{+0.007}_{-0.014}$	–	980^{+530}_{-119}	$-2.156^{+1.243}_{-1.327}$	100^{+85}_{-62}	$0.54^{+0.15}_{-0.21}$	–	–	–	–	–
Eureka!, $R = 400$	$1.304^{+0.005}_{-0.008}$	–	960^{+285}_{-93}	$-2.440^{+1.067}_{-1.242}$	123^{+78}_{-71}	$0.57^{+0.10}_{-0.18}$	–	–	–	–	–
<i>High Z solutions excluded</i>											
Tiberius, $R = 100$	$1.293^{+0.005}_{-0.017}$	–	933^{+293}_{-97}	$-3.772^{+1.511}_{-1.319}$	35^{+23}_{-19}	$0.49^{+0.15}_{-0.20}$	–	–	–	–	–
Tiberius, $R = 400$	$1.299^{+0.003}_{-0.005}$	–	852^{+84}_{-54}	$-2.539^{+0.915}_{-1.216}$	44^{+18}_{-21}	$0.51^{+0.12}_{-0.19}$	–	–	–	–	–
Eureka!, $R = 100$	$1.299^{+0.005}_{-0.011}$	–	923^{+195}_{-78}	$-2.141^{+1.213}_{-1.180}$	41^{+21}_{-22}	$0.57^{+0.11}_{-0.18}$	–	–	–	–	–
Eureka!, $R = 400$	$1.300^{+0.003}_{-0.005}$	–	915^{+77}_{-61}	$-2.469^{+1.010}_{-1.018}$	42^{+19}_{-21}	$0.61^{+0.07}_{-0.15}$	–	–	–	–	–

Table F1. WASP-15 parameters used in the UM simulations.

Parameter	Value	Unit
Type	F7	
Radius	10.03×10^8 ^a	m
Effective temperature	6300 ^b	K
Stellar constant at 1 au	4235.10	W m^{-2}
\log_{10} (surface gravity)	4.00 ^c	Gal (cgs)
[Fe/H]	0.00 ^d	dex

^a $10.03 \cdot 10^8 = 1.48 R_{\odot} \approx 1.477 \pm 0.072 R_{\odot}$ (Bonomo et al. 2017)

^b 6300 K $\approx 6372 \pm 13$ K (Gaia Collaboration et al. 2023)

^c 4.00 (cgs) ≈ 4.17 (cgs) (Bonomo et al. 2017)

^d 0.00 ≈ -0.17 (Bonomo et al. 2017)

Table F2. WASP-15b parameters used in the UM simulations.

Parameter	Value	Unit
Inner radius	9.07×10^7 ^a	m
Domain height	1.50×10^7 ^a	m
Semi-major axis	0.0520 ^b	au
Orbital period	3.7521 ^c	Earth day
Rotation rate	1.94×10^{-5}	rad s^{-1}
Surface gravity at inner radius	8.30 ^d	m s^{-2}
Intrinsic temperature	300	K
Metallicity [M/H]	10×solar	Asplund et al. (2009)
C/O	0.55	Asplund et al. (2009)
Specific gas constant	3256.02	$\text{J K}^{-1} \text{kg}^{-1}$
Specific heat capacity	1.25×10^4	$\text{J K}^{-1} \text{kg}^{-1}$
Stellar irradiance	1.57×10^6	W m^{-2}
Effective temperature	1555 ^e	K

^a $(9.07+1.50) \cdot 10^7 \text{ m} = 1.06 \cdot 10^8 \text{ m} = 1.48 R_{\text{J}}$

^b 0.0520 au ≈ 0.05165 au (Southworth et al. 2013)

^c 3.7521 Earth day ≈ 3.75209748 Earth day (Southworth et al. 2013)

^d With the inner radius boundary initially placed at 200 bar.

^e Calculated at pseudo-steady state as $(\text{OLR}/\sigma)^{1/4}$, where OLR is the global mean top-of-the-atmosphere outgoing longwave radiation and σ is the Stefan–Boltzmann constant.

APPENDIX F: ADDITIONAL DETAILS ABOUT THE UM

F1 WASP-15 system parameters used in the UM simulations

Tables F1 and F2 show the stellar and planetary parameters, respectively, used in the UM simulations presented in this study.

F2 UM initialisation and runtime

The UM equilibrium simulation was performed first. We initialised this simulation at rest with a piecewise power-law pressure-temperature profile crudely approximating the results from initial tests with analytic chemistry. This simulation was then ran for 1500 Earth days to let the upper atmosphere (from 10^{-3} bar to 1 bar) reach a pseudo-steady state dynamically, radiatively and chemically. The UM kinetics simulation was initialised from day 1000 of the UM equilibrium simulation, and ran for another 1000 Earth days.

F3 Constructing UM high resolution transmission spectrum

During normal UM runtime, radiative transfer is computed for 32 spectral bands covering 0.2 - 322 μm . During diagnostic UM runs required to obtain a planet’s transmission spectrum (Lines et al. 2018), radiative transfer was computed at a higher spectral resolution for two sets of spectral bands, (1) 500 spectral bands covering 0.2 - 10 000 μm and (2) 500 spectral bands covering 2 - 10 000 μm . The resulting two

Table G1. Line lists used to make PICASO Opacities.

Species	Reference
CO2	Huang et al. (2014)
CH4	Yurchenko et al. (2013b); Yurchenko & Tennyson (2014)
CO	Rothman et al. (2010a); Gordon et al. (2017a); Li et al. (2015b)
H2	Gordon et al. (2017a)
H2O	Polyansky et al. (2018b)
H2S	Azzam et al. (2016b)
H2–H2	Saumon et al. (2012); Lenzuni et al. (1991)
H2–He	Saumon et al. (2012)
H2–H	Saumon et al. (2012)
H2–CH4	Saumon et al. (2012)

high resolution transmission spectra were combined into one high resolution spectrum via post-processing.

F4 UM pressure-temperature and chemical species vertical profiles

Figure F1 shows pressure-temperature profiles predicted by the UM equilibrium and kinetics simulations for WASP-15b’s entire atmosphere and its terminator region (separately for the morning and evening terminators, i.e., exactly 90°E and 270°E , respectively, without averaging over the opening angle). The data were averaged over the last 200 simulation days.

APPENDIX G: ADDITIONAL DETAILS REGARDING PHOTOCHEMICAL MODELS

G1 Terminator Pressure/Temperature Profiles, K_{zz} Profile, and limb separated transmission spectra

The pressure/temperature profiles at the east and west limbs from the equilibrium UM GCM used for the photochemical modeling are shown in Figure G1 where we isothermally extend the atmospheric structure to high pressures where photochemistry is the most active. These profiles were averaged over $\pm 20^{\circ}$ of each terminator. The K_{zz} profile used in our modeling is also shown in Figure G1.

In the main text we show a limb-averaged transmission spectra for WASP-15b. In Figure G2 we show the transmission spectra separated for the east/west limbs for our best-fit 90× solar metallicity case. The SO₂ feature is visible on both limbs with an enhanced amplitude on the cooler west limb as was seen in Tsai et al. (2023).

G2 Molecular line lists used for PICASO opacities

The molecular line lists used to create the opacities in the PICASO radiative transfer modelling are given in Table G1.

This paper has been typeset from a $\text{\TeX}/\text{\LaTeX}$ file prepared by the author.

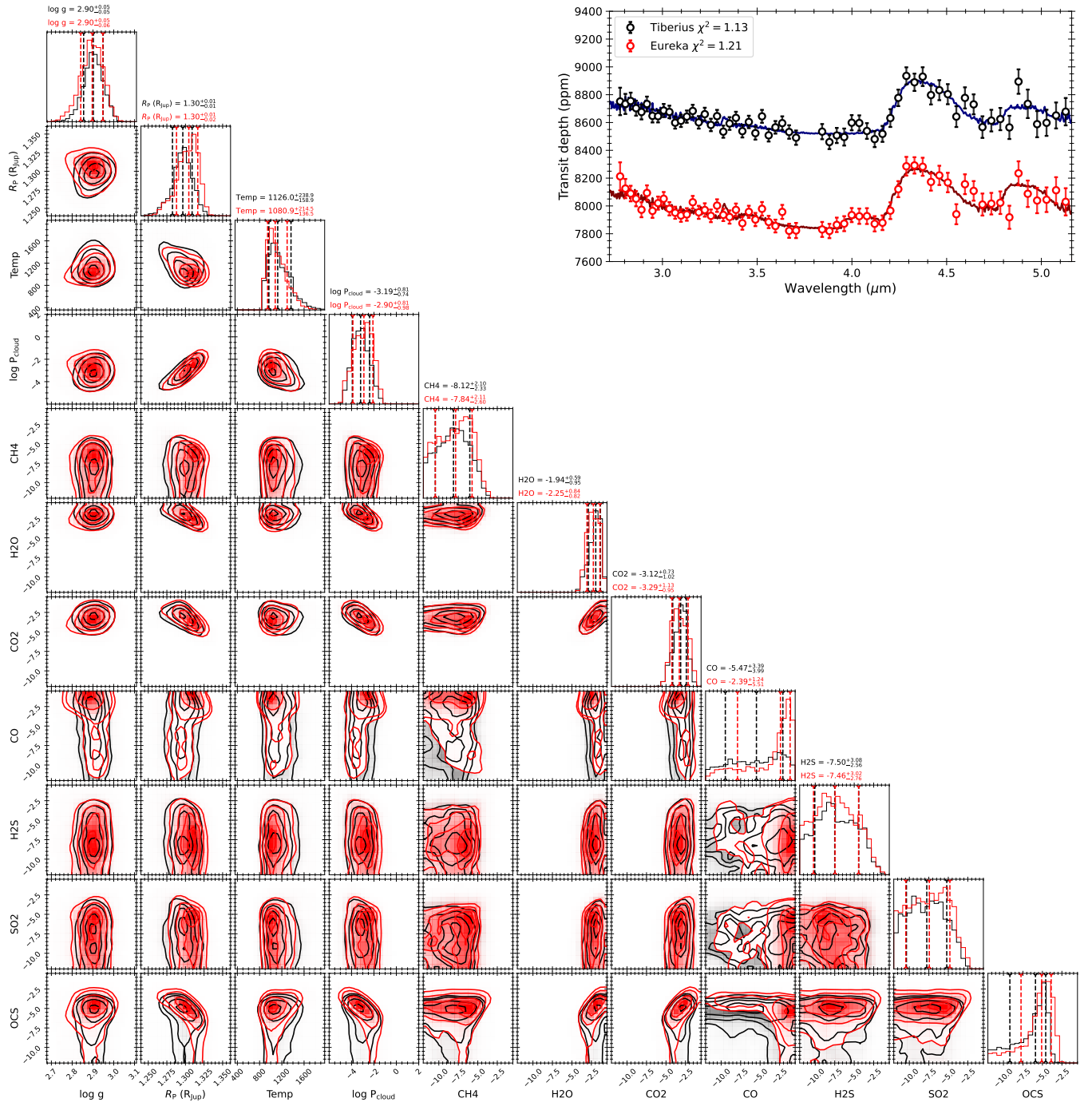


Figure E1. Corner plot showing the posterior PDFs from the free peti tRADTRANS retrieval performed on the Tiberius $R = 100$ spectrum (black) and Eureka! $R = 100$ spectrum (red). The best fitting model and residuals are displayed in the top right.

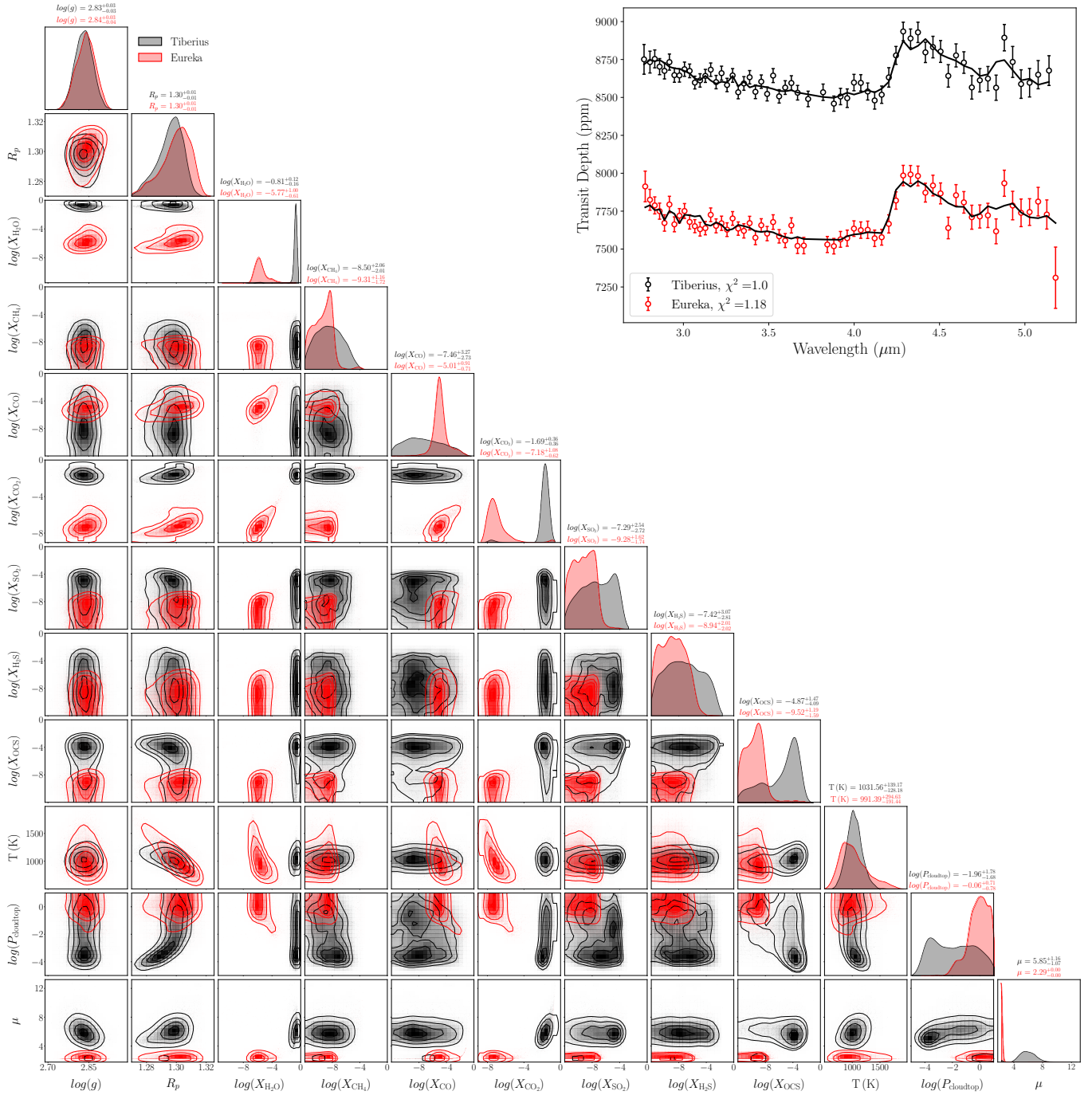


Figure E2. Cornerplot showing the posteriors from the BeAR retrievals on the Tiberius (black) and Eureka! (red) reductions of WASP-15 b at $R = 100$. Note that the mean molecular weight, μ , is not a free parameter in the retrievals, but is derived from the retrieved abundances. The top right insert shows the best-fit models for the Tiberius (black) and Eureka! (red) reductions. The Eureka! spectrum is offset by 1000 ppm for visualisation purposes. The legend in the bottom left indicates the reduced χ^2 values for each of the fits.

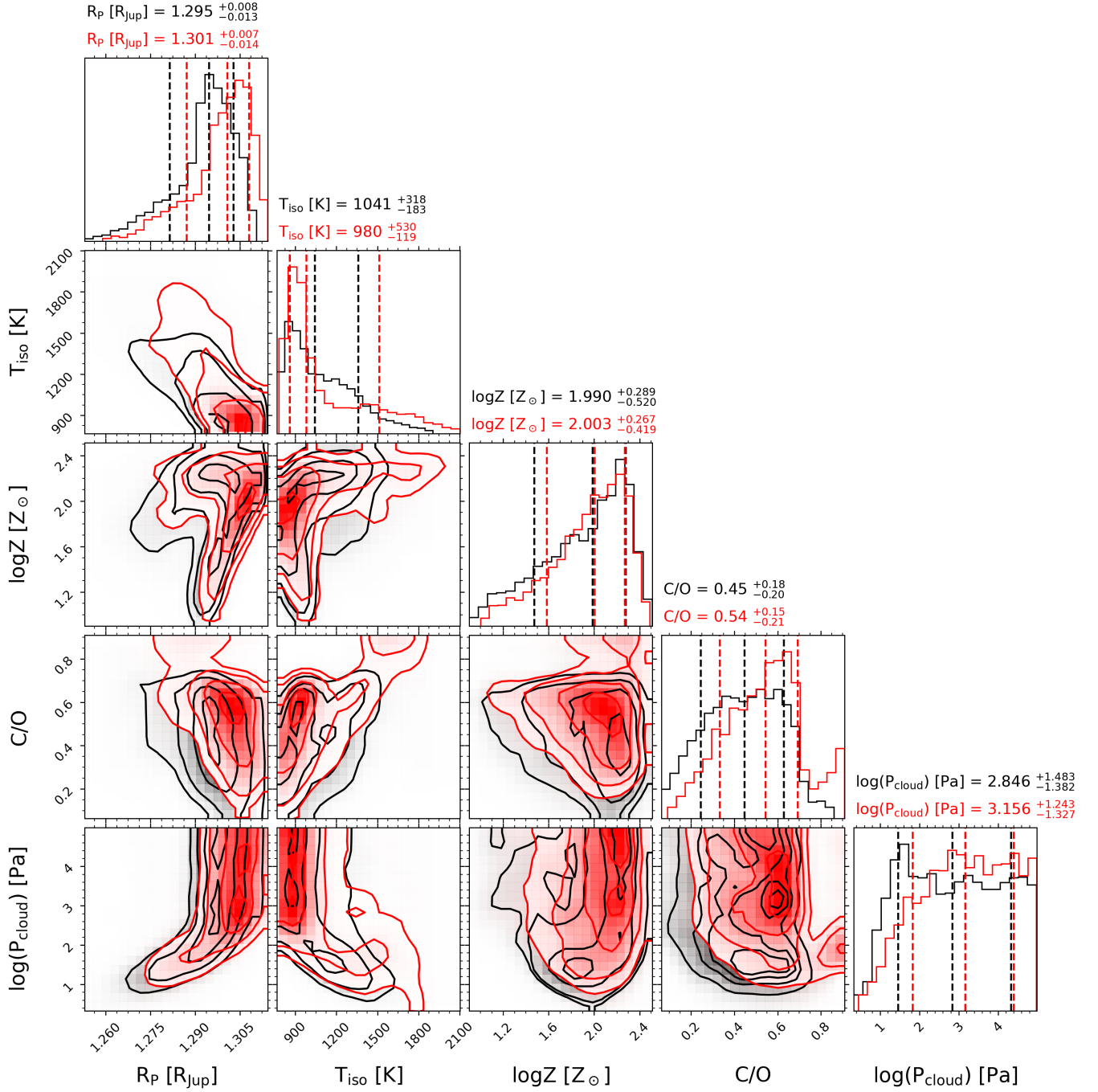


Figure E3. The corner plot from our 1D chemical equilibrium atmosphere retrievals with PLATON run on the $R = 100$ spectra over the full, unrestricted metallicity prior range $[-1, 3]$. The black contours correspond to the Tiberius retrieval and the red contours to the Eureka! retrieval. The vertical dashed lines indicate the 16th, 50th (median) and 84th percentiles, which are also given in the axes titles.

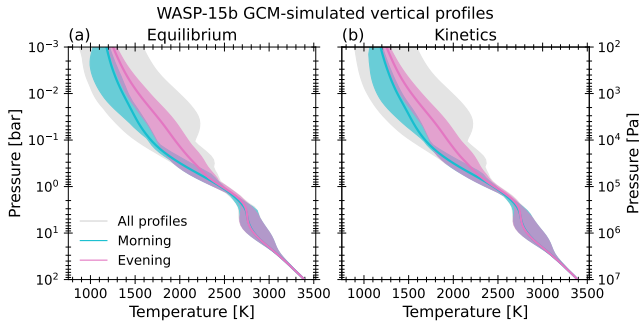


Figure F1. Pressure-temperature vertical profiles predicted by the UM equilibrium (left column) and kinetics (right column) simulations of WASP-15b’s atmosphere. Grey shading shows the range of abundances for the entire atmosphere, cyan shading — for the morning terminator only, pink shading — for the evening terminator only. Solid cyan and pink lines indicate the meridional mean for the morning and evening terminator, respectively.

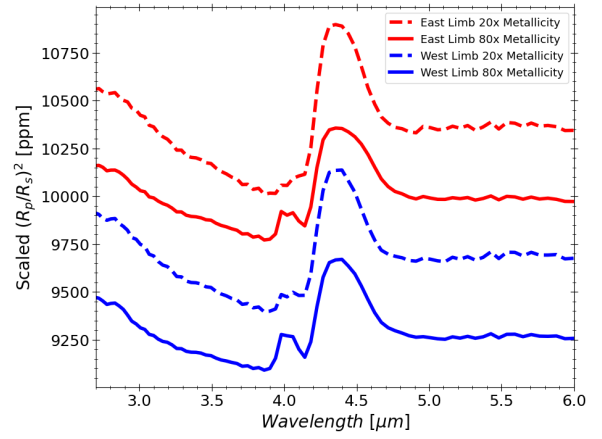


Figure G2. The limb separated transmission spectra based on the photochemical models for WASP-15b for both the 20 \times and 90 \times solar models.

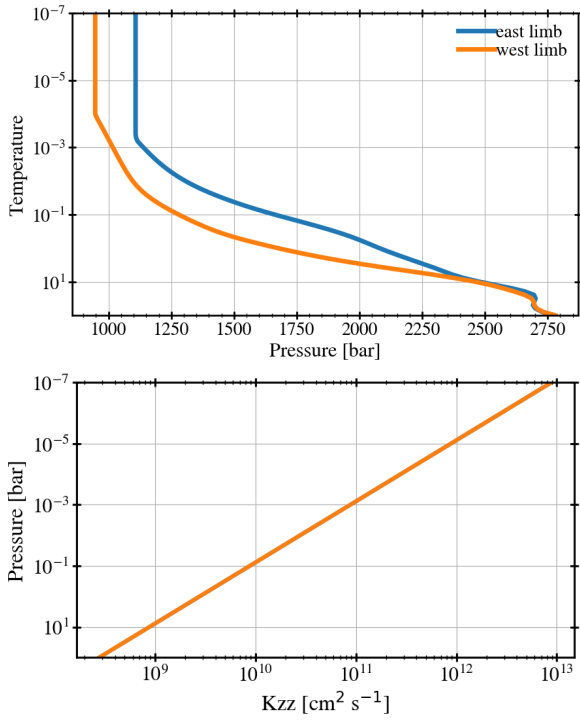


Figure G1. Top: the pressure/temperature profiles at the east and west terminators as calculated from the equilibrium UM GCM, Bottom: The K_{zz} profile used in the photochemical models.